Journal of Quantitative Spectroscopy & Radiative Transfer 240 (2020) 106683

Contents lists available at ScienceDirect

Journal of Quantitative Spectroscopy & Radiative Transfer

journal homepage: www.elsevier.com/locate/jqsrt

Assessing the accuracy and efficiency of longwave radiative transfer models involving scattering effect with cloud optical property parameterizations

Chia-Pang Kuo[a,b], Ping Yang[a,*], Xianglei Huang[c], Yi-Hsuan Chen[c], Guosheng Liu[b]

[a] Department of Atmospheric Sciences, Texas A&M University, College Station, TX, United States
[b] Department of Earth, Ocean and Atmospheric Science, Florida State University, Tallahassee, FL, United States
[c] Department of Climate and Space Sciences and Engineering, University of Michigan, Ann Arbor, MI, United States

ARTICLE INFO

Article history:
Received 6 August 2019
Revised 2 October 2019
Accepted 2 October 2019
Available online 4 October 2019

Keywords:
Radiative transfer
Water cloud parameterization
Ice cloud parameterization

ABSTRACT

A radiative transfer model (RTM) that accurately and explicitly accounts for both absorbing and scattering effects requires a substantial amount of computational effort. In the longwave (LW) spectral regime, the atmosphere is optically opaque and absorbs a large portion of terrestrial thermal radiation. To alleviate the computational burden, clouds are assumed to be only absorptive in most general circulation models (GCMs) and their scattering effects are neglected. Using parameterizations of cloud bulk single-scattering properties derived from the latest cloud optical property models for satellite remote sensing, this study analyzes the numerical accuracy and efficiency of a variety of LW RTMs . The approaches considered in this study include the absorption approximation (AA), the absorption approximation with scattering parameterization (ASA), the two-stream approximation (2S), a hybrid two- and four-stream approximation (2/4S), and the discrete ordinate radiative transfer (DISORT) with multiple streams. These approximations are benchmarked against 128-stream DISORT calculation. After evaluating the full ranges of ice and water cloud optical and microphysical properties using these RTMs, we find that neglecting LW scattering effect causes simulation errors as large as ±15% by using the AA method. Among these RTMs, the 2/4S method provides an optimal balance between computational efficiency and accuracy, leading to the maximum cloud emissivity errors within ±5%, 25th to 75th percentile errors about ±1%, and almost zero net bias. Therefore, the 2/4S approximation is computationally accurate and yet affordable option for incorporating cloud longwave scattering effect into the radiation schemes used in weather and climate models.

1. Introduction

General circulation models (GCMs) are extensively utilized in the study of our climate. Given the complexity of such models, and tremendous computational resources are required in simulating past climate and projecting future climate. In the longwave (LW) spectral regime, the atmosphere is relatively opaque; it absorbs and re-emits significant amount of terrestrial thermal radiation. As a result, LW absorption dominates over LW scattering. Because of strong atmospheric LW absorption and the fact that resolving LW scattering requires additional computational effort, most GCMs listed in Table 1 account for only LW absorption and neglect LW scattering to alleviate the computational burden. This simplification is implemented regardless of the presence of clouds [31-35].

Among the ten LW radiation schemes listed in Table 1, only three schemes, namely CanCM4 [1], HadCM3 [15], and GISS Model E and E2 [28,29], account for the cloud LW scattering effect. While LW scattering has been neglected in most mainstream GCMs, previous studies showed the importance of including LW scattering in model simulations. When LW scattering is neglected, Ritter and Geleyn [36] find an overestimation of 16 W/m^2 in the simulation of outgoing LW radiation (OLR) when a cloud is placed at altitudes between 12 and 13 km with liquid water content 0.01 g/m^2. In addition, Joseph and Min [37] analyze data from ground-based observations and show an overestimation of 6 to 8 W/m^2 in OLR when LW scattering is neglected. Moreover, using satellite data without consideration of LW scattering in off-line calculations, Costa and Shine [38] report an overestimation of OLR by approximately 3 W/m^2 from 60°N to 60°S. Similarly, Kuo et al. [33] find that OLR averaged between 85°N to 85°S is overestimated by 2.6 W/m^2 and the downward flux at the surface is underestimated by 1.2 W/m^2. For GCM applications, without inclusion of LW scattering, global

* Corresponding author.
E-mail address: pyang@tamu.edu (P. Yang).

https://doi.org/10.1016/j.jqsrt.2019.106683

Table 1
LW radiative transfer models in selected GCMs.

GCM	LW radiation scheme	Including LW scattering
CanCM4 [1]	2-stream approximation [2]	Yes
CAM4 [3]	Absorptivity/emissivity approximation [4]	No
CAM5 [5] CAM6 [6]	RRTMG_LW (2-stream approximation) [7-10]	No
CFSR [11] CFSv2 [12]	RRTMG_LW (2-stream approximation) [7-10]	No
ECHAM5 [13] ECHAM6 [14]	RRTMG_LW (2-stream approximation) [7-10]	No
HadCM3 [15]	2-stream approximation (PIFM) [16-19]	Yes
LMDZ4 [20]	Absorptivity/emissivity approximation [21]	No
LMDZ-B [22,23]	RRTMG_LW (2-stream approximation) [7-10]	No
GFDL Global Atmosphere Model AM2 [24] GFDL Global Atmosphere Model AM3 [25]	Absorptivity/emissivity approximation [26,27]	No
GISS ModelE [28] GISS ModelE2 [29]	Absorptivity/emissivity approximation with scattering effect correction [30]	Yes

Table 2
RRTMG_LW spectral bands.

Band	Wavenumber (cm^{-1})	Wavelength (μm)
1	10 - 350	1000.00 - 28.57
2	350 - 500	28.57 - 20.00
3	500 - 630	20.00 - 15.87
4	630 - 700	15.87 - 14.29
5	700 - 820	14.29 - 12.20
6	820 - 980	12.20 - 10.20
7	980 - 1080	10.20 - 9.26
8	1080 - 1180	9.26 - 8.47
9	1180 - 1390	8.47 - 7.19
10	1390 - 1480	7.19 - 6.76
11	1480 - 1800	6.76 - 5.56
12	1800 - 2080	5.56 - 4.81
13	2080 - 2250	4.81 - 4.44
14	2250 - 2380	4.44 - 4.20
15	2380 - 2600	4.20 - 3.85
16	2600 - 3250	3.85 - 3.08

OLR is overestimated, on average, by approximately 8 W/m^2 [39] or 1.5 W/m^2 [28], depending on the actual details of the model configurations. A recent study by Zhao et al. [35] suggests that including the cloud LW scattering in GCM simulations changes the circulation patterns; in particular, the Hadley circulation is amplified and the westerly jet is modified in the Southern Hemisphere while the precipitation in the tropical region is reduced.

Although previous studies [32,34,40] evaluate the performance of different radiative transfer models (RTMs) that can approximate the LW scattering, their assessments include limited microphysical and optical properties of ice or water clouds. In this study, to perform evaluations based on a broader range of microphysical and optical properties and thermodynamic phases of clouds, a range of ice and water clouds with different optical thickness (τ) and effective diameter (D_e) are used in several radiative transfer schemes to evaluate how accurate such schemes can be used for LW scattering calculation. Since the GCM version of the LW Rapid Radiative Transfer Model (RRTMG_LW) [7-10] is extensively used in the GCM applications listed in Table 1, this study develops the LW scattering properties of clouds, and evaluates the accuracy and efficiency of various RTMs with respect to the spectral bandwidths employed by the RRTMG_LW (Table 2). The optical properties of ice and water clouds and different RTMs are described in Section 2, and corresponding results and discussions are in Section 3. Finally, the conclusions of this study are given in Section 4.

2. Methodology

2.1. Parameterizations of cloud optical properties

RRTMG_LW considers cloud LW absorption but neglects cloud LW scattering [7-10]. In the present study, we compute the LW scattering properties of ice and water clouds for all the bands involved in the RRTMG_LW. The MODIS (Moderate Resolution Imaging Spectroradiometer) and CERES (Clouds and the Earth's Radiant Energy System) science teams respectively proposed different ice cloud optical models, which are referred to as the MODIS Collection 6 ice model (MC6) [41,42] and the two-habit models (THM) [43]. The MC6 ice cloud model consists of a single ice habit, which is a severely roughened aggregate of 8 hexagonal columns [41,42]. The THM consists of a mixture of individual roughened hexagonal columns and an ensemble of aggregates which is comprised of 20 randomly distorted hexagonal columns, and the mixing ratio of these two habits is a function of particle's maximum dimension [43]. To calculate the optical properties of individual ice crystals [44,45], both models utilize the invariant imbedding T-matrix method [46,47] for small to moderate particles, and the improved geometric optics method [48] with inclusion of the edge effect [45] for large particles. The refractive indices of ice are from Warren and Brandt [49]. To derive the bulk optical properties, modified gamma particle size distributions (PSDs) with an effective variance of 0.1 [42,43] and the Planck function at 233 K are used to integrate the single-scattering properties for these two models [50,51]. A significant advantage of using the two models is to achieve spectral consistency of optical thickness retrievals based on the MODIS solar and thermal infrared bands [41,42,52,53].

For water clouds, this study uses the MC6 spherical particle model [41,42]. The water refractive indices in the LW spectrum are from Downing and Williams [54], following Platnick et al. [42]. The single-scattering properties of water droplets are derived with the Lorenz-Mie theory [55]. The bulk optical properties of water clouds are also derived with the method described in Hong et al. [50] and Yi et al. [51], by weighting the single-scattering properties with modified gamma PSDs with an effective variance of 0.1 [42] and the Planck function at 300 K.

Because considerable computations are required in calculating the single-scattering properties and deriving the relevant bulk optical properties, a practical method to obtain the bulk optical properties in GCM applications is to parameterize the discrete bulk optical properties of ice and water clouds [50,51]. The ice and water cloud bulk mass extinction coefficient ($\bar{\kappa}_{ext}$), bulk single-scattering albedo ($\bar{\omega}$) and bulk asymmetry factor ($\bar{g}$) are parameterized in terms of the 3rd order polynomials for D_e larger than 20 μm and the 6th order polynomials for D_e smaller than 20 μm as a function of inverse D_e (D_{inv}). The definition of D_e and parameterizations of the bulk optical properties are as follows:

$$D_e = \frac{3\int_{D_{min}}^{D_{max}} V(D)N(D)dD}{2\int_{D_{min}}^{D_{max}} A(D)N(D)dD}, \tag{1}$$

$$D_{inv} = \frac{1}{D_e} - \frac{1}{20}, \tag{2}$$

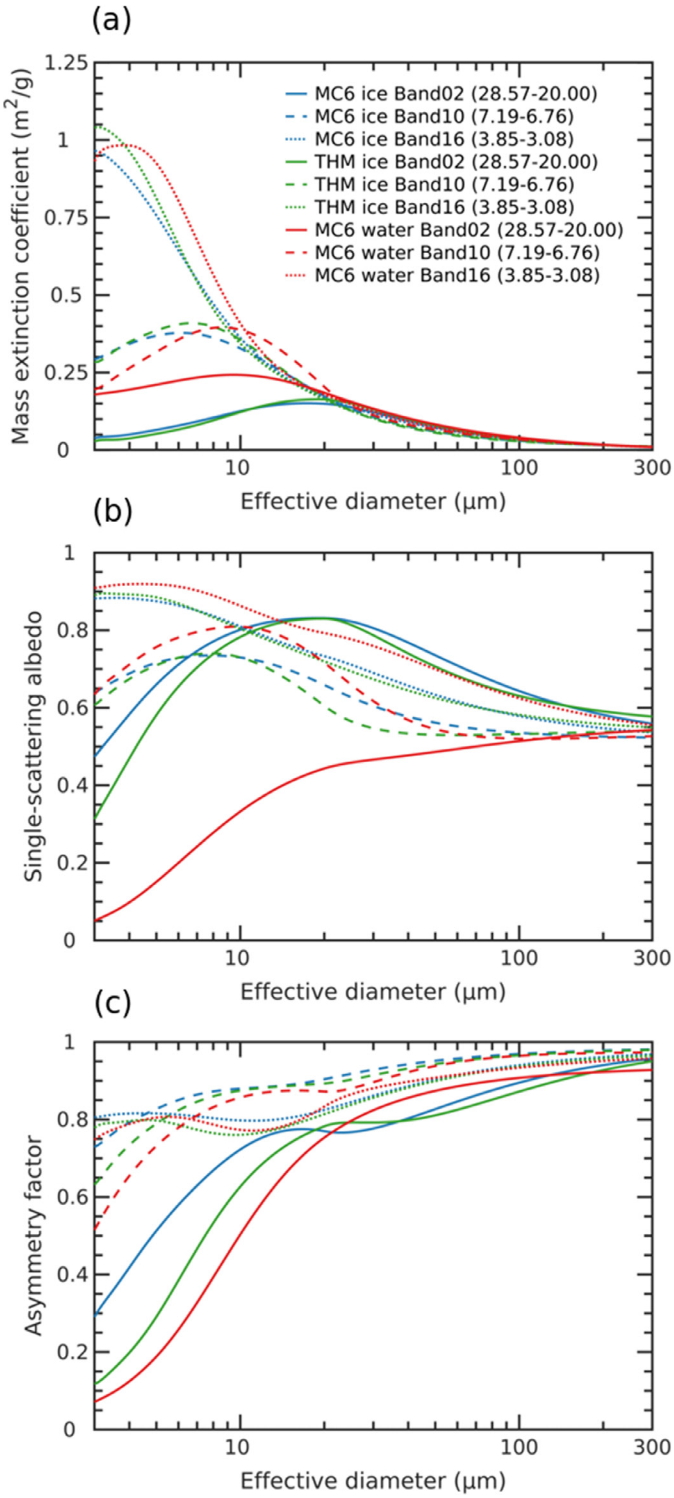

Fig. 1. Parameterized (a) $\bar{\kappa}_{ext}$ (m^2/g), (b) $\bar{\omega}$, and (c) $\bar{g}$ as functions of D_e in selected RRTMG_LW spectral bands. Blue, green, and red lines are for MC6 ice, THM ice, and MC6 water cloud models, respectively. Solid, dashed, and dotted lines indicate RRTMG_LW bands 2, 10, and 16, respectively. Numbers in parentheses are the spectral ranges for the bands in the wavelength domain.

$$\bar{\kappa}_{ext} = \begin{cases} \sum_{i=1}^{4} a_i (D_{inv})^{4-i}, & \text{for } D_e > 20\ \mu m \\ \sum_{i=1}^{7} a_i (D_{inv})^{7-i}, & \text{for } D_e \le 20\ \mu m \end{cases}, \tag{3}$$

$$\bar{\omega} = \begin{cases} \sum_{i=1}^{4} b_i (D_{inv})^{4-i}, & \text{for } D_e > 20\ \mu m \\ \sum_{i=1}^{7} b_i (D_{inv})^{7-i}, & \text{for } D_e \le 20\ \mu m \end{cases}, \text{ and} \tag{4}$$

$$\bar{g} = \begin{cases} \sum_{i=1}^{4} c_i (D_{inv})^{4-i}, & \text{for } D_e > 20\ \mu m \\ \sum_{i=1}^{7} c_i (D_{inv})^{7-i}, & \text{for } D_e \le 20\ \mu m \end{cases}, \tag{5}$$

where D is the particle maximum particle dimension, N is the particle number concentration, V and A are the volume and projected area for a particle, and a_i, b_i and c_i are the polynomial fitting coefficients for $\bar{\kappa}_{ext}$, $\bar{\omega}$ and $\bar{g}$, respectively. In addition, D_e in Eq. (1) may be expressed in terms of the ratio of mass to projected area [56]. Note that, as discussed in He et al. [57], different definitions of D_e, such as the volume-equivalent sphere diameter and the project-area-equivalent sphere diameter, can lead to different cloud optical properties.

In this study, the cloud optical property parameterizations are performed by fitting values of $\bar{\kappa}_{ext}$, $\bar{\omega}$ and $\bar{g}$ for 72 different D_e, particularly from 3 to 9 μm with a step size of 0.5 μm, 10 to 19 μm with a step size of 1 μm, and 20 to 500 μm with a step size of 10 μm. For MC6 ice, THM ice, and MC6 water cloud models, the parameterization processes and the corresponding root-mean-square errors (RMSEs) are shown in the appendix in Figs. A1 to A3 for fitting $\bar{\kappa}_{ext}$, Figs. A4 to A6 for fitting $\bar{\omega}$, and Figs. A7 to A9 for fitting $\bar{g}$. In Figs. A1 to A9, most RMSEs are in the order of 10^{-3} or less, indicating sufficient accuracy for radiative flux and cooling rate simulations. Although fitting $\bar{\omega}$ of THM ice clouds in the RRTMG_LW Band 2 (Fig. A5) show a RMSE as large as 10^{-2}, the spectral dependence of $\bar{\omega}$ is well represented by the fitted curve with acceptable fitting errors. Tables A1, A2, and A3 in the appendix list the values of polynomial fitting coefficients, which are valid when D_e is between 3 and 500 μm, for MC6 ice clouds, THM ice clouds, and MC6 water clouds, respectively.

Fig. 1 shows the parameterized bulk optical properties for MC6 and THM ice clouds, and MC6 water clouds as a function of D_e in several selected RRTMG_LW spectral bands. The optical properties of MC6 and THM ice clouds are similar, except for small D_e. For the MC6 water clouds, $\bar{\kappa}_{ext}$ is larger than for ice clouds in most cases. Water clouds have relatively larger $\bar{\omega}$ in the RRTMG_LW bands 10 and 16, but the contribution of these two bands to the LW flux and heating rate is order of magnitude smaller than that of RRTMG_LW band2. As suggested by Fig. 1, ice-cloud scattering effects are significantly larger than the water cloud counterparts in the RRTMG_LW band 2. This is consistent with previous results regarding the strong ice scattering effect around 25 μm [17, 33, 58]. As a result, the RRTMG_LW band2 can contribute about 40% of the bias in the simulated flux if LW scattering is ignored [33]. In RRTMG_LW bands 10 and 16, $\bar{g}$ is very similar for ice and water clouds. However, in RRTMG_LW band 2, comparing with water clouds, ice clouds have stronger forward scattering when D_e is less than 20 μm and have relatively weaker forward scattering for D_e larger than 20 μm.

2.2. Longwave radiative transfer models

For a plane-parallel atmosphere in local thermodynamic equilibrium, the general form of the LW radiative transfer equation [59,60] is expressed as follows:

$$\mu \frac{dI(\tau, \mu, \phi)}{d\tau} = I(\tau, \mu, \phi) - S(\tau, \mu, \phi), \text{ and} \tag{6a}$$

Table 3
Abbreviations of the RTMs.

Abbreviation	RTM
AA	Absorption approximation
ASA	Absorption approximation with scattering parameterization
2S	2-stream approximation
2/4S	2-/4-stream approximation
nSnM	n-stream DISORT with the H-G Phase function expanded from n moments of Legendre expansion coefficients

Table 4
The diffusivity factors and diffusivity coefficients used for the 2-stream approximations.

Method	$\tilde{D}$	χ
Hemispheric mean (HM) [62]	2	g
Modified 2-stream approximation [32]	1.66	G
Quadrature method (QM) [59]	$\sqrt{3}$	G
Practical improved flux method (PIFM) [19]	1.66	$\frac{3g}{2D}$

$$S(\tau,\mu,\phi) = \frac{\omega}{4\pi}\int_0^{2\pi}\int_{-1}^{1} P\left(\mu,\mu',\phi,\phi'\right) I\left(\tau,\mu',\phi'\right) d\mu' d\phi' + (1-\omega)B(T), \tag{6b}$$

where I is the diffuse radiance, μ is the cosine of the zenith angle θ, φ is the azimuth angle, S is the source function, ω is the single-scattering albedo, P is the phase function, and $B(T)$ is the Planck function at temperature T. Since solving the general radiative transfer equation requires significant computational resources, an efficient radiative solver is needed for GCMs.

From previous studies [19,32,40,59,61-63], a number of approximate approaches listed in Table 3 have been developed with different assumptions about the scattering phase function P. The simplest method may be the absorption approximation (AA) [32], which entirely neglects scattering in the radiative transfer. Alternatively, Chou et al. [40] proposed a method that applies the absorption approximation in conjunction with a scattering parameterization (ASA) scheme to incorporate the scattering effect into the AA. The ASA method increases τ of clouds to decrease upward and increase downward radiative flux, and the coefficients used to adjust τ are derived by parameterizing the scattering phase function [40].

A widely used approximate method for solving scattering radiative transfer is the 2-stream approximation (2S), which discretizes continuous radiation field into two radiation streams, one upward and one downward at a chosen zenith angle θ. Using τ as a vertical coordinate, the general form of the 2S approximations [32,61,63] can be stated as follows:

$$\begin{cases} \dfrac{dF^{+}(\tau)}{d\tau} = \gamma_1 F^{+}(\tau) - \gamma_2 F^{-}(\tau) - S^{+}(\tau) \\ \dfrac{dF^{-}(\tau)}{d\tau} = \gamma_2 F^{+}(\tau) - \gamma_1 F^{-}(\tau) + S^{-}(\tau) \end{cases}, \tag{7}$$

$$\gamma_1 = \tilde{D}\left[1 - \frac{\omega}{2}(1+\chi)\right], \tag{8}$$

$$\gamma_2 = \tilde{D}\frac{\omega}{2}(1-\chi), \text{ and} \tag{9}$$

$$S^{+}(\tau) = S^{-}(\tau) = \tilde{D}\pi(1-\omega)B(\tau), \tag{10}$$

where F is the radiative flux density or irradiance, $^{+}$ and $^{-}$ denote the upward and downward directions, respectively, $\tilde{D}$ is the diffusivity factor, which is inverse of μ ($\tilde{D} = 1/\mu$), and χ is the diffusivity coefficient. Table 4 lists values of $\tilde{D}$ and χ given by 4 different methods, including the hemispheric mean (HM) [62], the modified 2-stream approximation [32], the quadrature method (QM) [59], and the practical improved flux method (PIFM) [19]. To improve the 2S method, Fu et al. [32] proposed the 2-/4-stream approximation (2/4S), which is based on the source function technique described in Toon et al. [62]. The concept of 2/4S is to apply the 2S method to decompose S in Eq. (6b) analytically, and then, by using the specified S in Eq. (6a), I is separated into the upward and downward components. To obtain F, I is integrated over 4 angles (4-stream) based on the double Gaussian quadrature rule [32].

In this study, a comprehensive radiative transfer solver, DIScrete Ordinate Radiative Transfer (DISORT) [64], is used as the benchmark to validate approximate methods. DISORT discretizes the radiation field in terms of multiple streams in different directions. The more streams are used, the more accurate the results are. For this benchmark study, the Henyey-Greenstein (H-G) phase function [65] is assumed in DISORT, which can be expanded in terms of Legendre polynomials [59] as follows:

$$P_{HG}(cos\Theta) = \frac{1-g^2}{\left(1+g^2-2gcos\Theta\right)^{3/2}}, \text{ and} \\ = \sum_{l=0}^{L} w_l P_l(cos\Theta) \tag{11}$$

$$w_l = (2l+1)g^l, \tag{12}$$

where Θ is the scattering angle, and P_l and w_l indicate l moment of the Legendre polynomial and the corresponding Legendre polynomial expansion coefficient, respectively. In general, using the n-stream DISORT requires that P is reconstructed by at least n moments of Legendre expansion coefficients in the program. In this study, the benchmark is calculated by DISORT implemented with 128 streams and with 128 moments of Legendre expansion coefficients (128S128M).

To increase the accuracy of radiative transfer solver with a given number of streams, a technique called the δ-function adjustment is used to overcome issues caused by the strong forward scattering by clouds [66,67]. Based on the δ-function adjustment, the optical properties of clouds, specifically τ, ω, g, and w_l, are scaled as follows [32,59,60,66,67]:

$$\tau' = (1-\omega f)\tau, \tag{13}$$

$$\omega' = \frac{(1-f)\omega}{1-f\omega}, \tag{14}$$

$$g' = \frac{g-f}{1-f}, \text{ and} \tag{15}$$

$$w_l' = \frac{w_l - f(2l+1)}{1-f}, \tag{16}$$

where τ', ω', g', and w_l' are respectively the δ-function adjusted τ, ω, g, and w_l, and f is the truncation factor that describes the fraction of the scattered energy in the forward peak. In the case of an application of the H-G phase function to the n-stream approximation, f is determined by [59]

$$f = g^n. \tag{17}$$

Table 5
τ_{vis} and D_e in 840 combinations used for the present RTM comparisons.

τ_{vis}	D_e
0.1 to 0.9 with interval 0.1, 1 to 9 with interval 1, and 10 to 100 with interval 10	10 to 300 μm with interval 10 μm

3. Results and discussions

To mitigate the influence of atmosphere and temperature on the comparison results, based on the methodology described in Fu et al. [32], the ability of different RTMs to approximate the LW scattering effect is evaluated by using the cloud emissivity (ε_{cld}) for a given homogeneous isothermal cloud layer. The definition of ε_{cld} is the ratio of emitted flux to blackbody radiation with temperature *T*, and is given by

$$\varepsilon_{cld} = \frac{F}{\pi B(T)}, \tag{18}$$

where *T* is set at 273 K for both ice and water clouds in all radiative transfer simulations examined in this study. Since the centers of the emission bands shift from longer to shorter wavelengths with increasing *T* and clouds have various optical properties in different spectral bands, the values of ε_{cld} change with *T*. To quantity such variations with temperature, we use the benchmark 128S128M DISORT to compare ε_{cld} at 273 K with that of ice cloud at 233 K and with that of water cloud at 300 K. For both clouds, the ε_{cld} differences are less than 5%.

As far as evaluating the simulation is concerned, simulation errors are shown as a function of visible optical thickness (τ_{vis}), a convention widely used in the remote sensing of clouds and the cloud-radiation parameterization. In this study, the GCM version of the Shortwave Rapid Radiative Transfer Model (RRTMG_SW) [7-10] band 24 that spectrally ranges from 0.78 to 0.62 μm is selected to represent the visible band. In the RTM simulations, the value of τ for a given spectral band is obtained by

$$\tau_{band} = \frac{\bar{\kappa}_{ext}}{\bar{\kappa}_{ext,\ vis}} \tau_{vis}, \tag{19}$$

where τ_{band} is the optical thickness for a spectral band, and $\bar{\kappa}_{ext,\ vis}$ is the value of $\bar{\kappa}_{ext}$ in the RRTMG_SW band 24. The polynomial fitting coefficients of $\bar{\kappa}_{ext,\ vis}$ are also listed in Tables A1 to A3 in the appendix. After obtaining τ_{band}, the optical properties of clouds are scaled according to the δ-function adjustment mentioned in Section 2b, and then RTMs use scaled optical properties (τ'_{band}, ω'_{band}, and g'_{band} or $w'_{band,l}$) in each spectral band as input parameters to simulate ε_{cld}. In the assessment, the microphysical and optical properties of ice and water clouds correspond to 28 τ_{vis} values from 0.1 to 100 and 30 D_e values from 10 to 300 μm, totalling 840 combinations (Table 5).

Fig. 2 shows ε_{cld} calculated by using the 128S128M DISORT for ice and water clouds. When clouds become optically thick, they behave more like a blackbody and ε_{cld} is closer to unity. Fig. 1b shows that $\bar{\omega}$ first increases and then decreases with D_e; therefore, the scattering effects of both ice and water clouds are relatively strong when D_e is between 10 and 30 μm. Correspondingly, ε_{cld} in Fig. 2 increases with τ_{vis} and increases at first and then slightly decreases with D_e. When τ_{vis} is large enough (>4), ε_{cld} is close to 1.

To evaluate the accuracy of approximate methods over an extensive range of cloud microphysical and optical regimes, ε_{cld} is simulated by the methods listed in Table 3 with 840 combinations of τ_{vis} and D_e in Table 5 for ice and water clouds, and then is compared to ε_{cld} benchmark values. Using the optical properties of MC6 and THM ice clouds and MC6 water clouds, Fig. 3 shows the relative errors of emissivity for 22 RTMs, which include AA, ASA, 2S, and 2/4S with different $\tilde{D}$ values. In addition, to further compare with approximate models, the relative errors of cloud emissivity computed with 4 to 64 streams DISORT (4S4M to 64S64M) are also shown. As expected, the simulation accuracy increases with the number of streams used in the DISORT.

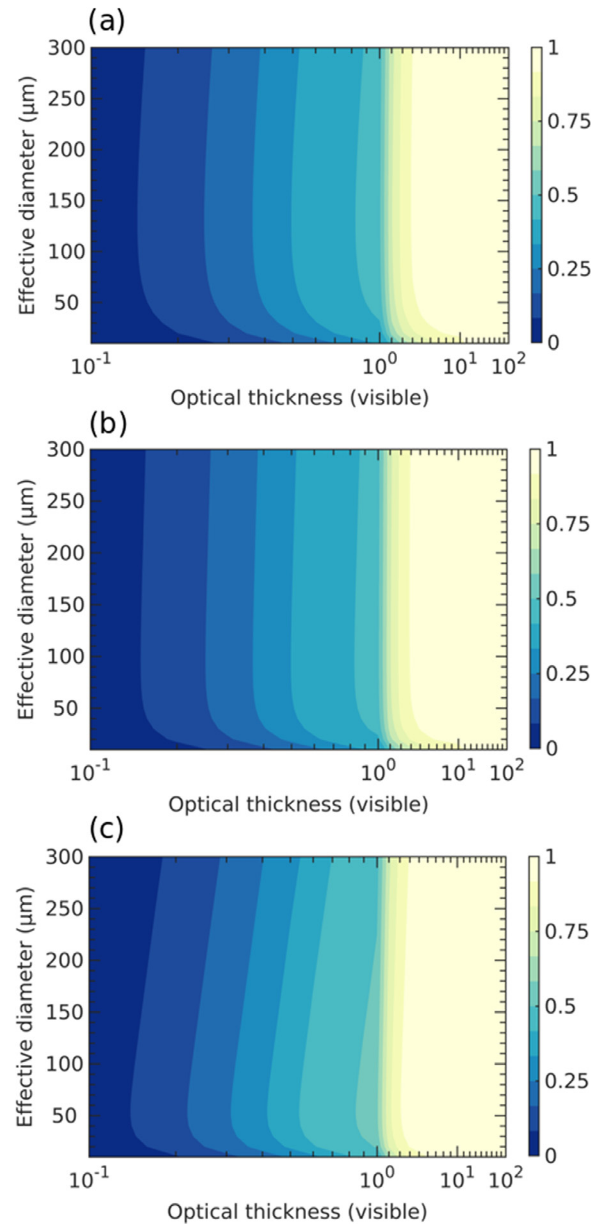

Fig. 2. Cloud layer emissivity simulated with the 128-stream DISORT as a function of τ_{vis} and D_e for (a) MC6 ice cloud model, (b) THM ice cloud model, and (c) MC6 water cloud model.

Water clouds in general have a weaker scattering effect than ice c louds, which explain why in Fig. 3 the relative errors of emissivity are slightly smaller for water clouds than for ice clouds. For the MC6 and THM ice clouds, the magnitudes of errors are comparable. Since distributions of the relative errors of emissivity are

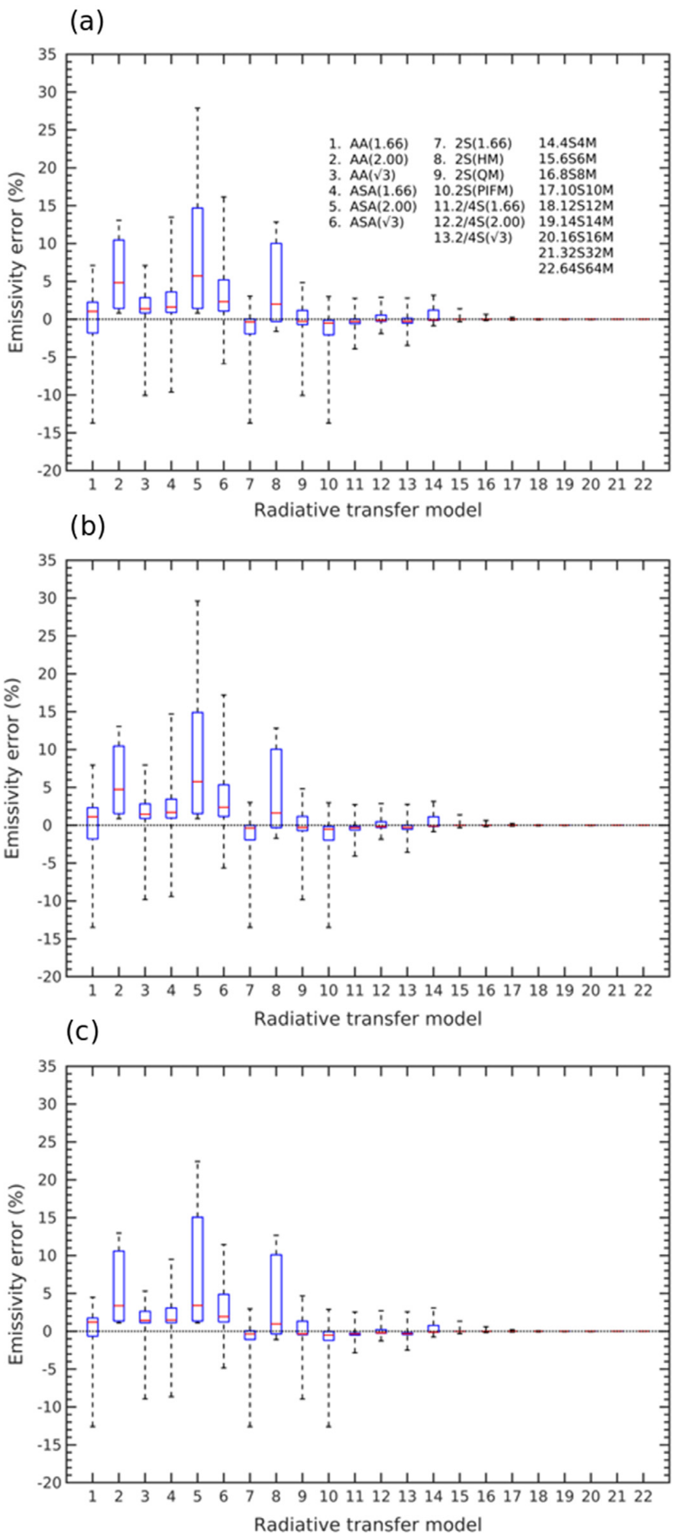

Fig. 3. Relative emissivity errors for (a) MC6 ice cloud model, (b) THM ice cloud model, and (c) MC6 water cloud model from 22 different RTMs listed in Table 3 in comparison to reference emissivity from 128-stream DISORT. The relative emissivity errors are calculated by 100 x (results from the approximate RTM – reference) / reference. In comparisons of 840 cases listed in Table 5, the upper and lower ends of the dashed whiskers indicate the extreme errors, top and bottom of the blue boxes are 25th and 75th percentiles, and red lines in the boxes indicate the median values. Numbers in parentheses are diffusivity factors. HM, QM, and PIFM refer to the hemispheric mean, the quadrature method, and the practical improved flux method, respectively. For models 14 to 22, nSnM means that DISORT is set in the n-stream (nS) mode with n moments (nM) of Legendre expansion coefficients.

similar for MC6 and THM ice clouds, Figs. 4 to 7 show the error distributions as a function of τ_{vis} and D_e only for MC6 ice and water clouds. While the error distributions between MC6 ice and water clouds are similar, the magnitudes of errors are larger for ice clouds than for water clouds.

Fig. 3 also shows that the AA and ASA approaches overestimate ε_{cld} in most cases, but the overall calculation errors are within $\pm$ 15%, except the case of ASA with $\tilde{D} = 2$ where the extreme error reaches 30% for ice clouds and all errors are overestimated. Fig. 4 shows the error distributions for MC6 ice and water clouds as a function of τ_{vis} and D_e for the AA method. When using AA, the simulated ε_{cld} is underestimated in the case of $\tau_{vis} < 1$ and is otherwise overestimated, except that ε_{cld} is always overestimated in the 840 cases using $\tilde{D} = 2$, with peak errors along $\tau_{vis} = 1$. In addition, for a given τ_{vis}, errors are larger when D_e is around 50 μm. While the value of $\tilde{D}$ is optimally set to 1.66 in the computation of the LW diffuse transmission [18,32], the corresponding simulation errors in these evaluations are moderate. Moreover, the error domains of extreme and 25th to 75th percentiles are smallest for ice or water clouds if $\tilde{D} = \sqrt{3}$ is assumed. Therefore, to improve simulation accuracy by using the AA method, the value of $\tilde{D}$ may be numerically optimized for different types of clouds.

The error patterns of the ASA method shown in Fig. 5, are very different from those of the AA method. Using ASA with $\tilde{D} = 1.66$ and $\sqrt{3}$ has positive extreme errors when τ_{vis} is around 1 and D_e is small, and has negative peak errors with small τ_{vis} and large D_e. When $\tilde{D} = 2$, using ASA overestimates all ε_{cld} values, similar to errors due to using the AA method, but the corresponding maximum error is around $\tau_{vis} \leq 2$ and $D_e \leq 30$ μm. Although the ASA method incorporates a LW scattering adjustment, Fig. 3 shows that the error space of the ASA is indeed larger than that of the AA. Since the adjusting coefficients described in Chou et al. [40] are designed for certain ice and water clouds, adjustments with the same coefficients are not suitable for the MC6 ice and water clouds and the THM ice clouds. Therefore, the ASA simulation errors here are larger than those without corrections.

While the maximum absolute errors $\sim$ 15% for the 2S shown in Fig. 3 are similar for the counterparts for the AA and ASA methods, the errors within the 25th to 75th percentiles are about 2% for 2S(1.66), 2S(QM), and 2S(PIFM), and corresponding median errors are very close to 0. Although the extreme error is also about 15% for 2S(HM), the 25th to 75th percentile error space (about 10%) and the median error (about 2%) are much larger than other 2S methods. Fig. 6 presents error distributions of different 2S methods as a function of τ_{vis} and D_e for MC6 ice and water clouds. The error patterns are similar between the AA and 2S methods, with the largest positive error around $\tau_{vis} = 1$ and negative errors for small τ_{vis}. Moreover, by using 2S(HM), ε_{cld} is almost exclusively overestimated in the entire optical and microphysical domain of clouds and the maximum error, which reaches 15%, is around $\tau_{vis} = 1$ with the error distribution essentially identical to the results for the AA with $\tilde{D}$=2.

While the error space is the largest with 2S(HM) compared to the other 2S methods, the justifications for using 2S(HM) are described by Edwards [68] and Toon et al. [62]. To derive the correct distribution of the Planck function for LW radiative transfer in an isothermal and large optical thickness atmospheric layer, $\tilde{D}$ should be 2. However, O'Brien et al. [63] argued against the usage of 2S(HM) and suggested that the correctly simulated Planck function distribution by using 2S(HM) is restricted to an interior point of a given layer and is not valid for a point close to boundary layers, where the angular distributions of the intensities significantly influence the scattering and emission processes. Figs. 3 and 6 support the arguments by O'Brien et al. [63] and numerically demonstrate that the simulation errors are smaller when 2S(1.66),

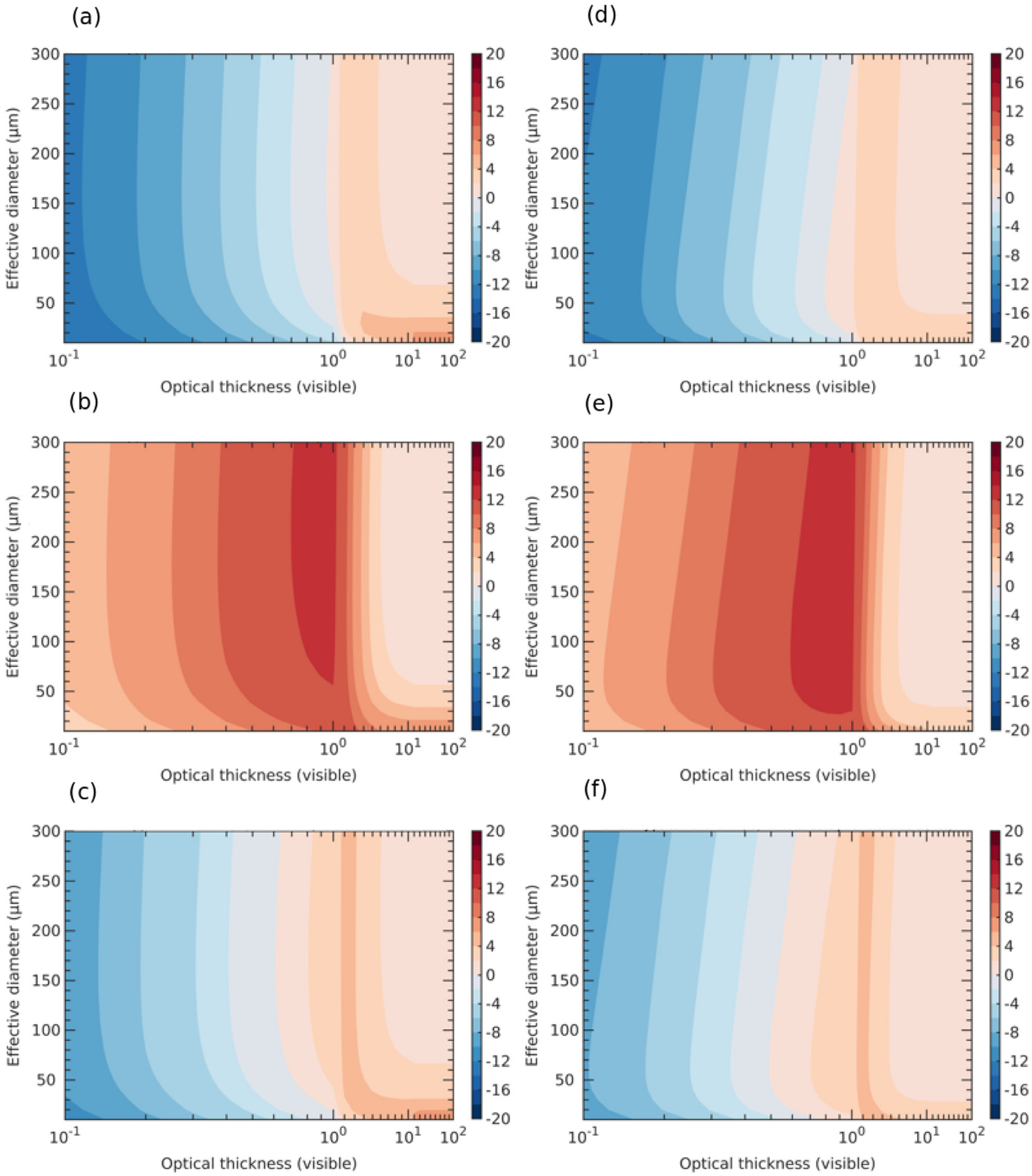

Fig. 4. Relative Emissivity errors as a function of τ_{vis} and D_e for MC6 ice (left column) and water (right column) clouds for approximation method (a) and (d) AA(1.66), (b) and (e) AA(2.00), and (c) and (f) AA($\sqrt{3}$). Color bars indicate relative error defined as 100 x (approximate results – reference) / reference. Numbers in parentheses are diffusivity factors.

2S(QM), and 2S(PIDM) are used instead of 2S(HM), because 2S(HM) significantly overestimates emissivity.

In contrast to AA, ASA, and 2S, Fig. 7 shows that the errors of 2/4S are the largest when τ_{vis} is small and D_e is large, and have large negative errors around $\tau_{vis} = 1$ when D_e is small. Furthermore, Fig. 3 shows that the extreme errors of the 2/4S method are much smaller and simulated ε_{cld} is significantly less biased than other approximation methods. As mentioned in Liou [59], using 2/4S with different $\tilde{D}$ values all provide accurate results that are supported by Fig. 3, because all of the 2/4S error spaces are about the same. All 2/4S approaches have the largest positive errors around 3%, but the extreme negative error is slightly smaller for $\tilde{D} = 2$ (−2%) than for $\tilde{D} = 1.66$ and $\sqrt{3}$, which are about −4% and −3%, respectively.

As shown in Fig. 3, in which simulation errors with 4- to 64-stream DISORT are compared with other approximation methods,

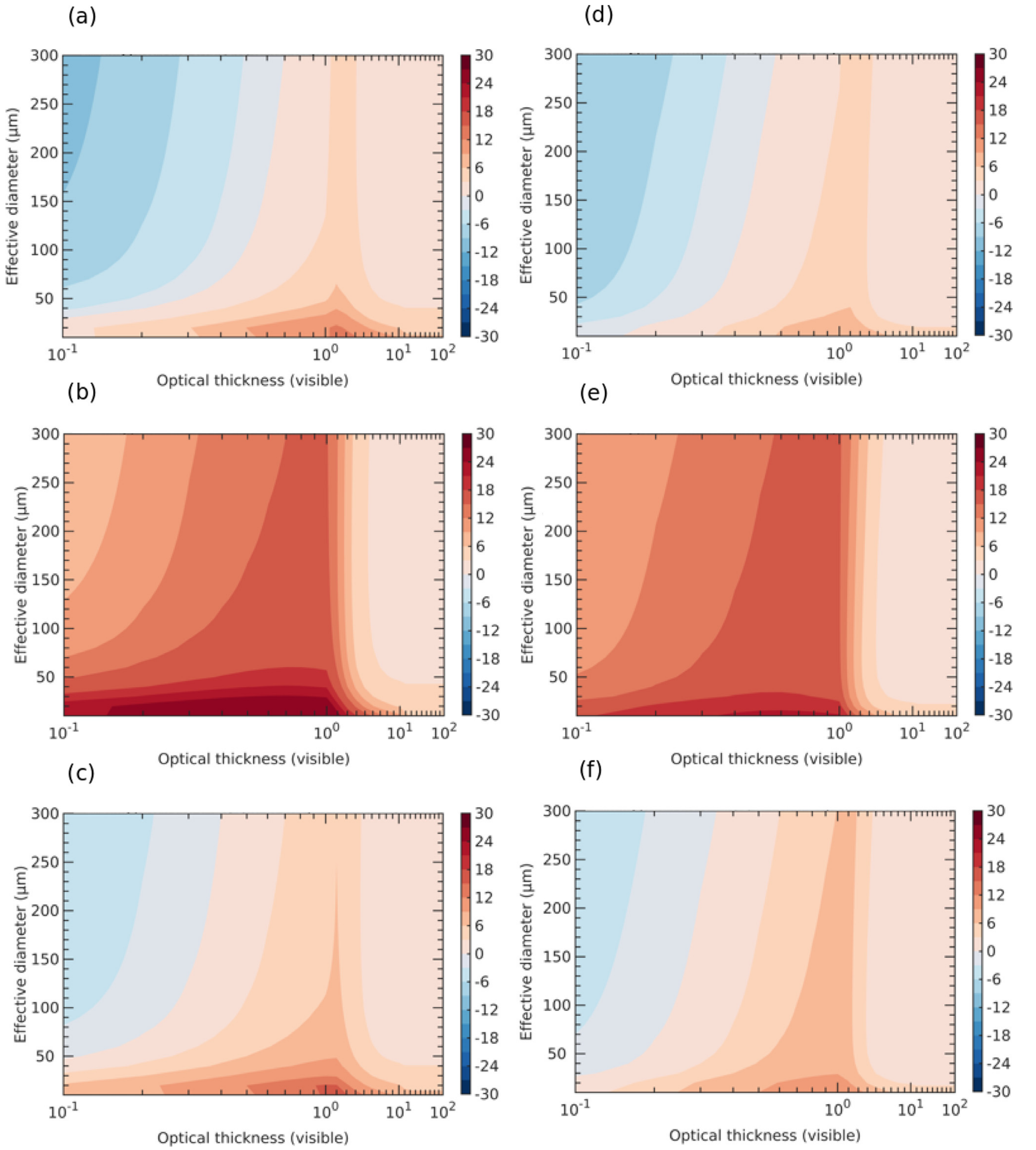

Fig. 5. Same as Fig. 4, except for relative emissivity errors for MC6 ice (left column) and water (right column) clouds for approximation methods: (a) and (d) ASA(1.66), (b) and (e) ASA(2.00), and (c) and (f) ASA($\sqrt{3}$).

the peak errors are about 3%, 2%, and 1% with 4S4M, 6S6M, and 8S8M DISORT, respectively, and simulation errors are negligible when stream number is larger than 10. When comparing 2/4S and 4S4M DISORT, the error patterns shown in Fig. 7 are similar. In addition, ε_{cld} is overestimated around smaller τ_{vis} and larger D_e, and underestimated when $\tau_{vis} = 1$ with small D_e. Although the largest negative error is reduced by using 4S4M DISORT, the range of 25th to 75th percentile errors are much smaller for 2/4S approximations (Fig. 3).

To evaluate the simulation efficiency of different RTMs, the computational time is averaged over 1000 runs of AA, 2S and 2/4S modules, and over 100 executions of the nSnM DISORT subroutine for the cases of MC6 ice clouds. Fig. 8 shows the simulation accuracy and efficiency of different RTMs, including 4S4M to 16S16M DISORT, and AA, 2S and 2/4S with the most accurate results for

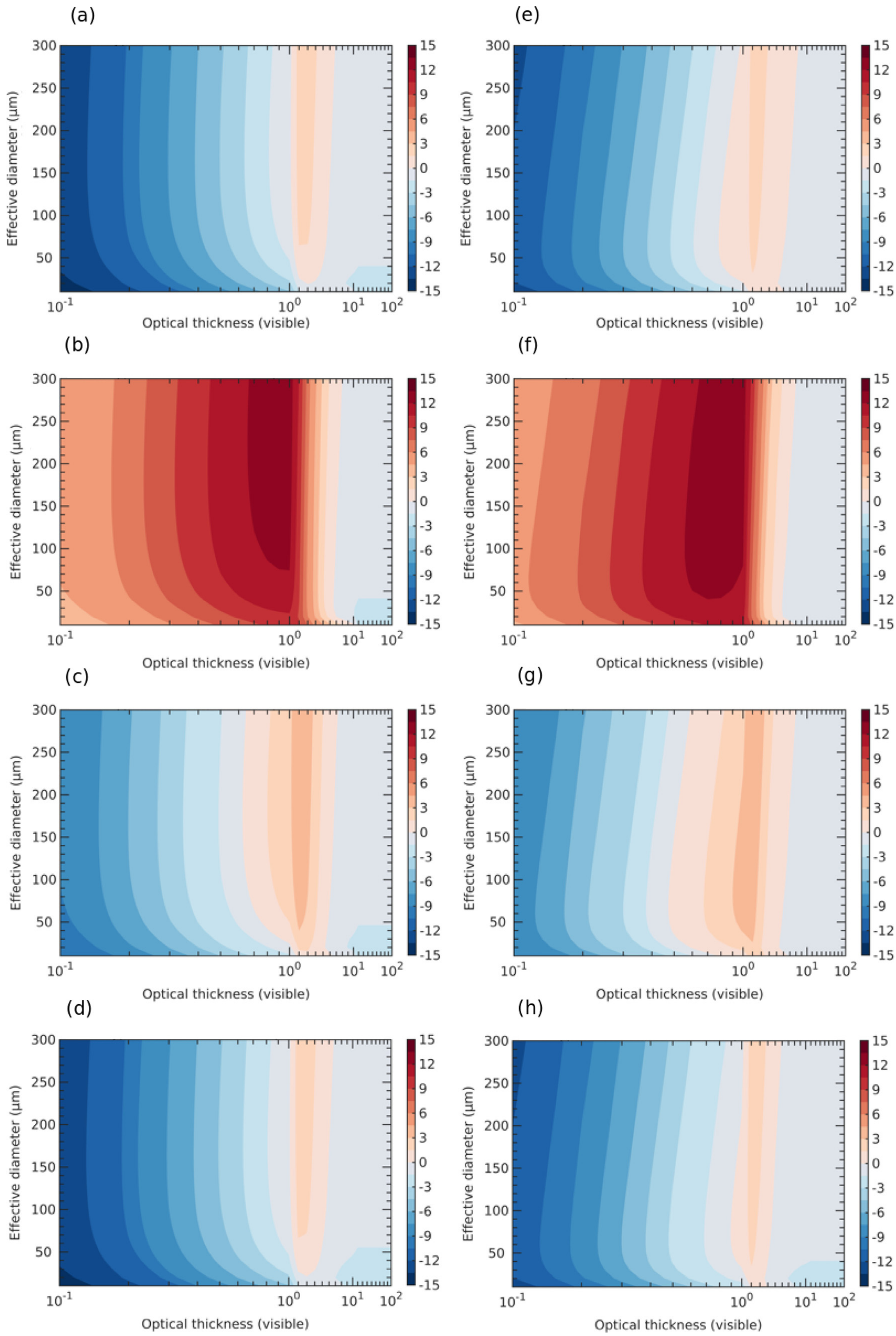

Fig. 6. Same as Fig. 4, except for relative emissivity errors for MC6 ice (left column) and water (right column) clouds for approximation methods: (a) and (e) 2S(1.66), (b) and (f) 2S(HM), (c) and (g) 2S(QM), and (d) and (h) 2S(PIFM). HM, QM, PIFM in parentheses refer to the hemispheric mean, quadrature method, and practical improved flux method, respectively.

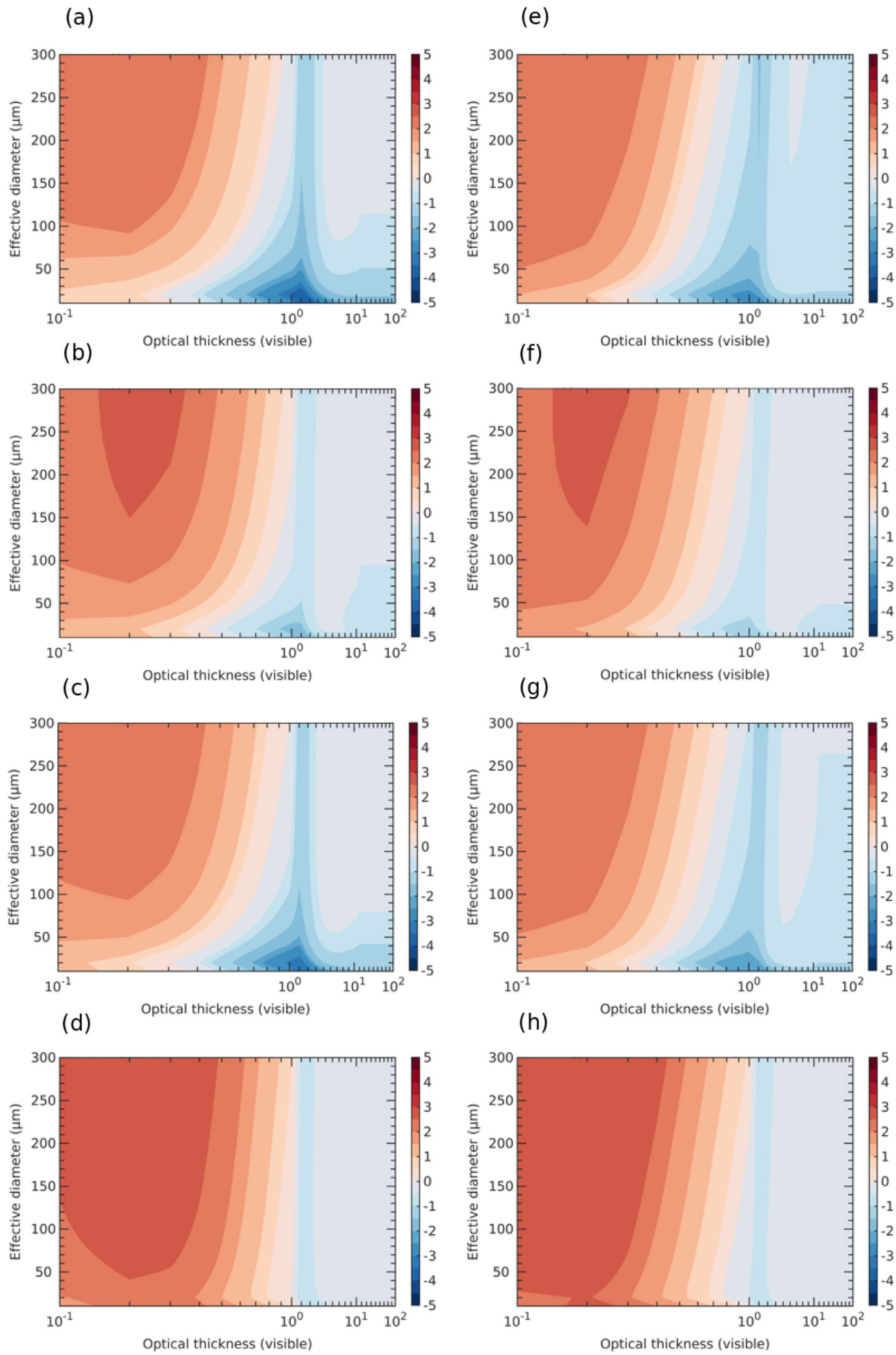

Fig. 7. Same as Fig. 4, except for relative emissivity errors for MC6 ice (left column) and water (right column) clouds for approximation methods: (a) and (e) 2/4S(1.66), (b) and (f) 2/4S(2.00), (c) and (g) 2/4S($\sqrt{3}$), and (d) and (h) 4S4M DISORT.

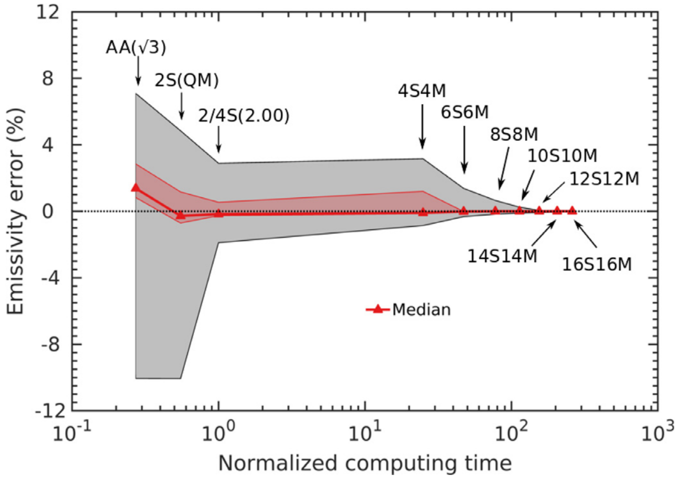

Fig. 8. Relative Emissivity errors as a function of normalized computing time for AA($\sqrt{3}$), 2S(QM), 2/4S(2.00), and 4S4M to 16S16M DISORT. Red line with triangle mark denotes median values of relative emissivity error. Grey area presents the maximum error space, and red region shows the errors in the 25th to 75th percentiles. Numbers in parentheses are diffusivity factors, and QM means the quadrature method.

each approximation method. ASA is omitted in the Fig. 8 because its computational time is about the same as for AA, but ASA has larger simulation errors as mentioned in previous paragraphs. Moreover, the mean calculating times in Fig. 8 are normalized with respect to averaged execution time of the 2/4S module. As expected, more accurate simulations generally take much longer. For example, by using 4S4M to 16S16M DISORT, the extreme simulation errors reduce from 3% to nearly 0% but the computing time increases by a factor from 25 to 250. The mean execution times for AA and 2S are respectively about 0.3 and 0.5 times compared to 2/4S, but both cannot achieve the same accuracy as the 2/4S. While 4S4M DISORT has a slightly smaller error space than 2/4S, 2/4S has a smaller range of 25th to 75th percentile errors and only take 1/25 as much time as required by the 4S4M DISORT.

4. Conclusions

Most mainstream GCMs listed in Table 1 only account for absorption processes in the LW radiative transfer. As a prerequisite of evaluating the climate consequences of neglecting LW scattering, this study thoroughly analyzes the accuracy and efficiency of various RTMs by using the latest cloud optical property models, specifically MC6 ice and water clouds and THM ice clouds, over a full range of cloud microphysical and optical properties. To avoid the complexity of calculating cloud single-scattering properties and deriving the corresponding bulk cloud optical properties by weighting the single-scattering properties, a practical method widely adopted by the GCM development is to use parameterizations of the cloud bulk optical properties, including $\bar{\kappa}_{ext}$, $\bar{\omega}$, and $\bar{g}$ shown in Fig. 1 with relevant polynomial coefficients listed in Tables A1 to A3.

By using the comprehensive microphysical and optical properties of ice and water clouds, for different RTMs, including AA, ASA, 2S, 2/4S, and DISORT (with 128 streams as the most accurate reference), accuracy is evaluated by errors of simulated ε_{cld}, and normalized computational times are used to assess the efficiency of RTM modules in the domain of τ_{vis} from 0.1 to 100 and D_e from 10 to 300 μm. The extreme errors of AA are all within ± 15% with different $\tilde{D}$ values. The ASA method compensates for the LW scattering effect by increasing cloud optical thickness, but the publically available adjusting coefficients are not designed for MC6 and THM ice clouds and MC6 water clouds. As a result, the ASA approaches here are less accurate than using AA, and the relevant maximum error is about 30% for ice clouds, and is the largest among all of the approximate methods examined here.

With the 2S methods, the best overall simulations are provided by 2S(QM) with extreme errors about - 10%, and 25th to 75th percentile errors are about 4% with a bias about - 1%. Finally, 2/4S approximations obtain the overall best results among all approximate methods: the largest errors are decreased from ±15% (AA, ASA, and 2S) to ±5%, and the 25th to 75th percentile error range is reduced to within ±1%. As far as the DISORT is concerned, as expected, the larger the number of streams is, the more accurate the results are. The errors are essentially trivial when more than 10 streams are used.

Other than accuracy of the RTMs, computational efficiency is another important factor that we evaluate for the possible implementation in the large-scale climate model simulations. Overall, Fig. 8 clearly shows that simulation errors decrease with increasing computational effort from AA to DISORT. While the DISORT provides the most accurate results, the computational time is 20- 200 times longer than the 2/4S. In consistent with the findings of Fu et al. [32] and Liou [59], this study confirms that the best trade-off between accuracy and efficiency is to use the 2/4S combination in a GCM application.

Declaration of Competing Interest

None

Acknowledgments

This study was supported by the National Science Foundation (AGS-1632209). PY also acknowledges support by the endowment funds (02-512231-10000) related to the David Bullock Harris Chair in Geosciences at the College of Geosciences, Texas A&M University. The computational resources used in this study are provided by the Texas A&M Supercomputing Facility (http://sc.tamu.edu).

Supplementary materials

Supplementary material associated with this article can be found, in the online version, at doi:10.1016/j.jqsrt.2019.106683.

Appendix: Parameterization coefficients and errors

Figs. A1–A10, Tables A1–A3

Table A1
Polynomial fitting coefficients a_i, b_i and c_i for $\bar{\kappa}_{ext}$, $\bar{\omega}$ and $\bar{g}$, respectively, in 16 RRTMG_LW bands, and coefficients a_i for $\bar{\kappa}_{ext}$ in RRTMG_SW band 24, for the MC6 ice cloud optical model.

Band	20 μm	$\bar{\kappa}_{ext}$ polynomial fitting coefficients (a_i) for MC6 ice cloud						
		$i=1$	$i=2$	$i=3$	$i=4$	$i=5$	$i=6$	$i=7$
1	>	4.0049E+01	−3.4075E+01	6.3608E-02	9.1957E-02	N/A	N/A	N/A
	≤	−1.2237E+03	1.1269E+03	−4.0310E+02	6.9880E+01	−5.6558E+00	6.3608E-02	9.1957E-02
2	>	−5.8789E+02	−8.2308E+01	4.3728E-01	1.4945E-01	N/A	N/A	N/A
	≤	−6.1032E+03	5.7521E+03	−2.1259E+03	3.8542E+02	−3.2967E+01	4.3728E-01	1.4945E-01
3	>	−2.0345E+01	−1.1970E+01	3.2052E+00	1.8295E-01	N/A	N/A	N/A
	≤	−2.9679E+03	3.4516E+03	−1.6563E+03	4.1896E+02	−5.7215E+01	3.2052E+00	1.8295E-01
4	>	−8.1835E+00	7.9568E+00	3.9870E+00	1.7827E-01	N/A	N/A	N/A
	≤	2.5457E+03	−1.8647E+03	3.2956E+02	7.2422E+01	−3.4334E+01	3.9870E+00	1.7827E-01
5	>	−1.0961E+01	1.8769E+00	3.4032E+00	1.6399E-01	N/A	N/A	N/A
	≤	1.9708E+03	−1.7728E+03	5.6017E+02	−4.7844E+01	−1.3019E+01	3.4032E+00	1.6399E-01
6	>	−1.9887E+01	−1.4072E+01	1.9537E+00	1.2997E-01	N/A	N/A	N/A
	≤	−2.4607E+02	3.0245E+02	−1.6437E+02	5.4009E+01	−1.2291E+01	1.9537E+00	1.2997E-01
7	>	−4.5200E+01	−3.0277E+01	1.6817E+00	1.4908E-01	N/A	N/A	N/A
	≤	−2.4415E+03	2.5899E+03	−1.1284E+03	2.5947E+02	−3.2575E+01	1.6817E+00	1.4908E-01
8	>	−4.9305E-01	−1.0176E+01	3.0941E+00	1.7586E-01	N/A	N/A	N/A
	≤	−1.9728E+03	2.3080E+03	−1.1398E+03	3.0629E+02	−4.6394E+01	3.0941E+00	1.7586E-01
9	>	−1.4206E+00	1.0173E+01	4.1136E+00	1.7997E-01	N/A	N/A	N/A
	≤	8.0692E+02	−3.1945E+02	−1.9615E+02	1.5792E+02	−4.1066E+01	4.1136E+00	1.7997E-01
10	>	1.6785E+01	1.9194E+01	4.3521E+00	1.7383E-01	N/A	N/A	N/A
	≤	3.0947E+03	−2.6231E+03	7.2892E+02	−2.4253E+01	−2.5812E+01	4.3521E+00	1.7383E-01
11	>	1.6649E+01	1.9492E+01	4.2963E+00	1.7066E-01	N/A	N/A	N/A
	≤	3.7798E+03	−3.3671E+03	1.0620E+03	−1.0084E+02	−1.7561E+01	4.2963E+00	1.7066E-01
12	>	5.1665E+01	2.7884E+01	4.5145E+00	1.6655E-01	N/A	N/A	N/A
	≤	7.5560E+03	−7.0795E+03	2.5173E+03	−3.8069E+02	5.1471E+00	4.5145E+00	1.6655E-01
13	>	4.7000E+00	9.2164E+00	3.7195E+00	1.6467E-01	N/A	N/A	N/A
	≤	7.8849E+03	−7.7360E+03	2.9901E+03	−5.4340E+02	3.0837E+01	3.7195E+00	1.6467E-01
14	>	2.6101E+00	3.2265E+00	3.4495E+00	1.6460E-01	N/A	N/A	N/A
	≤	7.0258E+03	−7.0549E+03	2.8235E+03	−5.4321E+02	3.5904E+01	3.4495E+00	1.6460E-01
15	>	−6.9625E+00	−7.0280E+00	3.0532E+00	1.6695E-01	N/A	N/A	N/A
	≤	4.9157E+03	−5.3302E+03	2.3461E+03	−5.0965E+02	4.1749E+01	3.0532E+00	1.6695E-01
16	>	−6.3289E-01	−7.0828E+00	3.0930E+00	1.6949E-01	N/A	N/A	N/A
	≤	−3.5978E+03	2.5284E+03	−4.1789E+02	−7.4449E+01	1.9322E+01	3.0930E+00	1.6949E-01
24	>	6.2000E+00	2.2901E+00	3.2960E+00	1.5978E-01	N/A	N/A	N/A
	≤	−1.1553E+03	9.2469E+02	−2.4033E+02	2.2151E+01	2.3790E-01	3.2960E+00	1.5978E-01
Band	**20 μm**	**$\bar{\omega}$ polynomial fitting coefficients (b_i) for MC6 ice cloud**						
		$i=1$	$i=2$	$i=3$	$i=4$	$i=5$	$i=6$	$i=7$
1	>	5.9731E+02	−1.7237E+01	−4.1624E+00	4.3766E-01	N/A	N/A	N/A
	≤	−2.1616E+03	1.8638E+03	−5.4594E+02	3.3498E+01	1.5870E+01	−4.1624E+00	4.3766E-01
2	>	1.1835E+03	−6.7633E+01	1.0648E-01	8.3148E-01	N/A	N/A	N/A
	≤	−1.9794E+03	1.8390E+03	−6.9282E+02	1.4743E+02	−2.0063E+01	1.0648E-01	8.3148E-01
3	>	−2.0168E+03	−1.4582E+02	9.0066E-01	6.9216E-01	N/A	N/A	N/A
	≤	−1.7669E+03	1.7377E+03	−7.1008E+02	1.6541E+02	−2.4572E+01	9.0066E-01	6.9216E-01
4	>	−6.2926E+02	−3.1906E+01	9.6178E-01	5.8403E-01	N/A	N/A	N/A
	≤	−1.8865E+03	1.7528E+03	−6.6834E+02	1.4567E+02	−2.1328E+01	9.6178E-01	5.8403E-01
5	>	−1.0260E+01	4.7744E+00	−5.4265E-01	5.0373E-01	N/A	N/A	N/A
	≤	−8.6302E+02	7.2819E+02	−2.4176E+02	4.5242E+01	−5.5503E+00	−5.4265E-01	5.0373E-01
6	>	−2.0263E+01	−1.2346E+01	−2.2538E+00	4.5416E-01	N/A	N/A	N/A
	≤	−6.0318E+02	4.1723E+02	−7.1723E+01	−1.3374E+01	8.1424E+00	−2.2538E+00	4.5416E-01
7	>	−1.1958E+03	−1.3184E+02	2.2394E-01	6.9715E-01	N/A	N/A	N/A
	≤	−2.5536E+03	2.4170E+03	−9.2697E+02	1.9083E+02	−2.2614E+01	2.2394E-01	6.9715E-01
8	>	−2.1404E+03	−1.7037E+02	1.4760E+00	7.4871E-01	N/A	N/A	N/A
	≤	−4.4149E+03	4.1076E+03	−1.5194E+03	2.9250E+02	−3.3089E+01	1.4760E+00	7.4871E-01
9	>	−1.8419E+03	−1.2451E+02	2.4175E+00	7.2336E-01	N/A	N/A	N/A
	≤	−5.4780E+03	5.1329E+03	−1.9153E+03	3.7169E+02	−4.2419E+01	2.4175E+00	7.2336E-01
10	>	−6.3032E+02	−2.8190E+01	2.9644E+00	6.5886E-01	N/A	N/A	N/A
	≤	−5.1567E+03	4.9127E+03	−1.8798E+03	3.7912E+02	−4.5769E+01	2.9644E+00	6.5886E-01
11	>	−2.1501E+01	1.1373E+01	3.0544E+00	6.3672E-01	N/A	N/A	N/A
	≤	−4.3463E+03	4.2058E+03	−1.6462E+03	3.4340E+02	−4.3564E+01	3.0544E+00	6.3672E-01
12	>	5.0579E-01	−3.1888E+01	3.7056E+00	7.7148E-01	N/A	N/A	N/A
	≤	−4.9953E+03	4.9350E+03	−1.9726E+03	4.1550E+02	−5.1165E+01	3.7056E+00	7.7148E-01
13	>	6.6483E+00	7.4423E+00	3.7800E+00	6.8763E-01	N/A	N/A	N/A
	≤	9.2176E+02	−2.9206E+02	−2.1677E+02	1.4135E+02	−3.3228E+01	3.7800E+00	6.8763E-01
14	>	−8.5067E+00	7.6067E+00	3.5544E+00	6.7398E-01	N/A	N/A	N/A
	≤	3.1843E+03	−2.3607E+03	5.1467E+02	1.6547E+01	−2.3067E+01	3.5544E+00	6.7398E-01
15	>	−3.8891E+01	−3.6648E+01	2.9397E+00	7.4331E-01	N/A	N/A	N/A
	≤	3.2133E+03	−2.5127E+03	6.3376E+02	−2.2702E+01	−1.6204E+01	2.9397E+00	7.4331E-01

(*continued on next page*)

Table A1 (*continued*)

16	>	−2.9277E+01	−5.5820E+01	1.6778E+00	7.3323E-01	N/A	N/A	N/A
	≤	2.4399E+03	−2.2974E+03	8.0992E+02	−1.1964E+02	1.3444E+00	1.6778E+00	7.3323E-01
Band	20 μm	$\bar{g}$ polynomial fitting coefficients (c_i) for MC6 ice cloud						
		$i=1$	$i=2$	$i=3$	$i=4$	$i=5$	$i=6$	$i=7$
1	>	−8.3171E+00	7.8161E+00	−4.0810E+00	7.3656E-01	N/A	N/A	N/A
	≤	−6.4315E+02	8.8207E+02	−4.8279E+02	1.1643E+02	−3.4222E+00	−4.0810E+00	7.3656E-01
2	>	−5.5533E+02	8.4619E+01	1.1465E+00	7.6991E-01	N/A	N/A	N/A
	≤	−1.0229E+04	9.7252E+03	−3.6525E+03	6.9337E+02	−6.8540E+01	1.1465E+00	7.6991E-01
3	>	1.2272E+03	1.1133E+02	−4.4995E-01	8.2211E-01	N/A	N/A	N/A
	≤	2.6249E+03	−1.8978E+03	4.0801E+02	3.9064E+00	−1.1201E+01	−4.4995E-01	8.2211E-01
4	>	6.6545E+01	1.0239E+01	−1.4213E+00	8.7282E-01	N/A	N/A	N/A
	≤	3.6272E+03	−3.1552E+03	1.0265E+03	−1.4828E+02	8.0816E+00	−1.4213E+00	8.7282E-01
5	>	8.7751E+00	−1.1088E+00	−1.1394E+00	8.9907E-01	N/A	N/A	N/A
	≤	1.7607E+03	−1.4767E+03	4.4673E+02	−5.3184E+01	8.5139E-01	−1.1394E+00	8.9907E-01
6	>	7.8437E+00	−3.6678E+00	−1.3029E+00	9.2074E-01	N/A	N/A	N/A
	≤	4.6731E+03	−4.0641E+03	1.3186E+03	−1.9073E+02	1.0835E+01	−1.3029E+00	9.2074E-01
7	>	7.7900E+00	5.7682E+00	−2.0928E+00	8.7817E-01	N/A	N/A	N/A
	≤	1.7294E+04	−1.5810E+04	5.5244E+03	−9.0414E+02	6.5181E+01	−2.0928E+00	8.7817E-01
8	>	2.9585E+02	3.3311E+01	−1.6906E+00	8.6246E-01	N/A	N/A	N/A
	≤	1.6497E+04	−1.5036E+04	5.2392E+03	−8.5429E+02	6.0604E+01	−1.6906E+00	8.6246E-01
9	>	6.1530E+02	4.8336E+01	−1.3907E+00	8.7383E-01	N/A	N/A	N/A
	≤	1.2316E+04	−1.1217E+04	3.9143E+03	−6.4241E+02	4.6261E+01	−1.3907E+00	8.7383E-01
10	>	1.4522E+02	1.5116E+01	−1.2642E+00	9.0385E-01	N/A	N/A	N/A
	≤	7.2935E+03	−6.6758E+03	2.3563E+03	−3.9664E+02	3.0341E+01	−1.2642E+00	9.0385E-01
11	>	7.0414E+00	6.9444E+00	−1.1042E+00	9.1623E-01	N/A	N/A	N/A
	≤	5.5697E+03	−5.0881E+03	1.7962E+03	−3.0419E+02	2.3743E+01	−1.1042E+00	9.1623E-01
12	>	5.9141E+02	7.7077E+01	−6.5728E-01	8.4182E-01	N/A	N/A	N/A
	≤	1.0720E+04	−9.5782E+03	3.2680E+03	−5.2329E+02	3.6291E+01	−6.5728E-01	8.4182E-01
13	>	2.9727E+02	3.0026E+01	−1.4113E+00	8.7861E-01	N/A	N/A	N/A
	≤	7.5058E+03	−6.9154E+03	2.4799E+03	−4.3462E+02	3.7004E+01	−1.4113E+00	8.7861E-01
14	>	1.4597E+02	1.4426E+01	−1.6398E+00	8.8701E-01	N/A	N/A	N/A
	≤	6.3517E+03	−5.9773E+03	2.2100E+03	−4.0581E+02	3.7422E+01	−1.6398E+00	8.8701E-01
15	>	1.3284E+02	3.0335E+01	−1.7662E+00	8.4271E-01	N/A	N/A	N/A
	≤	7.0581E+03	−6.7560E+03	2.5502E+03	−4.7930E+02	4.5056E+01	−1.7662E+00	8.4271E-01
16	>	−2.2494E+00	2.8366E+01	−1.7573E+00	8.2451E-01	N/A	N/A	N/A
	≤	3.9087E+03	−4.0511E+03	1.6837E+03	−3.5533E+02	3.8435E+01	−1.7573E+00	8.2451E-01

Table A2
As in Table A1 but for the THM ice cloud optical model.

Band	20 μm	$\bar{k}_{ext}$ polynomial fitting coefficients (a_i) for THM ice cloud						
		$i=1$	$i=2$	$i=3$	$i=4$	$i=5$	$i=6$	$i=7$
1	>	−9.3065E+00	−4.0733E+01	−6.2702E-02	9.5493E-02	N/A	N/A	N/A
	≤	−1.4808E+03	1.3492E+03	−4.7427E+02	7.9156E+01	−5.6336E+00	−6.2702E-02	9.5493E-02
2	>	−1.2108E+03	−1.2192E+02	2.2833E-01	1.6332E-01	N/A	N/A	N/A
	≤	−9.0250E+03	8.3395E+03	−2.9909E+03	5.1611E+02	−4.0144E+01	2.2833E-01	1.6332E-01
3	>	−1.0947E+01	2.0297E+00	4.0715E+00	1.9450E-01	N/A	N/A	N/A
	≤	−5.7789E+03	6.3480E+03	−2.8540E+03	6.6869E+02	−8.3063E+01	4.0715E+00	1.9450E-01
4	>	1.5303E+01	2.1907E+01	4.6742E+00	1.8309E-01	N/A	N/A	N/A
	≤	6.0743E+03	−4.7287E+03	1.1325E+03	−6.2204E-01	−3.8515E+01	4.6742E+00	1.8309E-01
5	>	7.9244E+00	5.5117E+00	3.6222E+00	1.6839E-01	N/A	N/A	N/A
	≤	4.0417E+03	−3.6556E+03	1.2103E+03	−1.4869E+02	−7.9874E+00	3.6222E+00	1.6839E-01
6	>	−1.9937E+01	−1.3885E+01	2.0559E+00	1.3426E-01	N/A	N/A	N/A
	≤	−2.7917E+02	3.1847E+02	−1.6559E+02	5.4239E+01	−1.2696E+01	2.0559E+00	1.3426E-01
7	>	−2.9011E+02	−3.9210E+01	2.0941E+00	1.6321E-01	N/A	N/A	N/A
	≤	−6.4682E+03	6.2719E+03	−2.4325E+03	4.8264E+02	−5.0639E+01	2.0941E+00	1.6321E-01
8	>	1.7833E+01	1.6276E+01	4.3934E+00	1.8227E-01	N/A	N/A	N/A
	≤	−4.2969E+03	4.9153E+03	−2.3074E+03	5.6911E+02	−7.6277E+01	4.3934E+00	1.8227E-01
9	>	2.7717E+02	4.7470E+01	5.1385E+00	1.7619E-01	N/A	N/A	N/A
	≤	7.7805E+03	−5.8893E+03	1.3535E+03	5.7941E+00	−4.4361E+01	5.1385E+00	1.7619E-01
10	>	1.2891E+01	2.4927E+01	4.5175E+00	1.6954E-01	N/A	N/A	N/A
	≤	1.5225E+04	−1.3251E+04	4.2142E+03	−5.3425E+02	1.8259E+00	4.5175E+00	1.6954E-01
11	>	1.7815E+01	1.6361E+01	4.0612E+00	1.6696E-01	N/A	N/A	N/A
	≤	1.5664E+04	−1.4091E+04	4.7309E+03	−6.7620E+02	1.9058E+01	4.0612E+00	1.6696E-01
12	>	−5.6012E-01	−8.6710E+00	2.9691E+00	1.6743E-01	N/A	N/A	N/A
	≤	1.9434E+04	−1.9132E+04	7.2555E+03	−1.2626E+03	7.7593E+01	2.9691E+00	1.6743E-01
13	>	−1.3745E+02	−2.4978E+01	2.5148E+00	1.6747E-01	N/A	N/A	N/A
	≤	−2.1436E+03	−1.0430E+03	1.8015E+03	−6.0249E+02	5.9839E+01	2.5148E+00	1.6747E-01
14	>	−1.9241E+01	−1.6107E+01	2.6537E+00	1.6661E-01	N/A	N/A	N/A
	≤	−9.5127E+03	5.5871E+03	−4.1805E+02	−2.7800E+02	4.3032E+01	2.6537E+00	1.6661E-01
15	>	−8.3173E+00	−5.8160E+00	3.0774E+00	1.6558E-01	N/A	N/A	N/A
	≤	−2.1493E+04	1.6673E+04	−4.2494E+03	3.0350E+02	1.0778E+01	3.0774E+00	1.6558E-01

(*continued on next page*)

Table A2 (*continued*)

16	>	−1.4930E+00	1.1825E+01	3.8114E+00	1.6306E-01	N/A	N/A	N/A
	≤	−1.5596E+04	1.4447E+04	−4.8522E+03	6.5400E+02	−2.6396E+01	3.8114E+00	1.6306E-01
24	>	−6.7089E+00	4.3614E-01	3.2051E+00	1.5832E-01	N/A	N/A	N/A
	≤	5.2938E+02	−4.1562E+02	1.0643E+02	−1.4677E+01	1.7648E+00	3.2051E+00	1.5832E-01
Band	20 μm	$\bar{\omega}$ polynomial fitting coefficients (b_i) for THM ice cloud						
		$i=1$	$i=2$	$i=3$	$i=4$	$i=5$	$i=6$	$i=7$
1	>	−5.9426E+02	−7.3581E+01	−4.7982E+00	4.1057E-01	N/A	N/A	N/A
	≤	−2.5757E+03	2.2847E+03	−7.0421E+02	5.5082E+01	1.7579E+01	−4.7982E+00	4.1057E-01
2	>	−1.2574E+03	−1.7390E+02	4.3428E-02	8.3022E-01	N/A	N/A	N/A
	≤	−4.2382E+03	3.7715E+03	−1.3172E+03	2.4733E+02	−2.9414E+01	4.3428E-02	8.3022E-01
3	>	−2.7928E+03	−1.2950E+02	2.6138E+00	6.6289E-01	N/A	N/A	N/A
	≤	−9.4790E+03	8.9758E+03	−3.3761E+03	6.5484E+02	−7.1121E+01	2.6138E+00	6.6289E-01
4	>	−2.8462E+01	6.1289E+01	2.8464E+00	5.3254E-01	N/A	N/A	N/A
	≤	−2.9074E+03	3.2705E+03	−1.5152E+03	3.7668E+02	−5.3675E+01	2.8464E+00	5.3254E-01
5	>	−2.3084E+00	2.9563E+01	−7.3786E-02	4.6745E-01	N/A	N/A	N/A
	≤	2.3078E+03	−1.8446E+03	4.9371E+02	−3.2036E+01	−6.4089E+00	−7.3786E-02	4.6745E-01
6	>	−1.4935E+02	−1.0681E+01	−1.9708E+00	4.3625E-01	N/A	N/A	N/A
	≤	−5.0511E+02	4.8280E+02	−1.7456E+02	2.4634E+01	2.3989E+00	−1.9708E+00	4.3625E-01
7	>	−2.5815E+03	−1.7324E+02	1.0381E+00	6.9823E-01	N/A	N/A	N/A
	≤	−6.7838E+03	6.3711E+03	−2.3846E+03	4.5987E+02	−4.7978E+01	1.0381E+00	6.9823E-01
8	>	−1.8632E+03	−1.0474E+02	3.1954E+00	7.3219E-01	N/A	N/A	N/A
	≤	−1.0119E+04	9.4963E+03	−3.5369E+03	6.7521E+02	−7.1772E+01	3.1954E+00	7.3219E-01
9	>	−2.5597E+00	3.4928E+01	4.6511E+00	6.8305E-01	N/A	N/A	N/A
	≤	−9.1963E+03	8.9347E+03	−3.4871E+03	7.0898E+02	−8.2137E+01	4.6511E+00	6.8305E-01
10	>	2.3547E+02	8.3923E+01	4.7998E+00	6.0494E-01	N/A	N/A	N/A
	≤	−1.6195E+03	2.3490E+03	−1.3270E+03	3.8405E+02	−6.2200E+01	4.7998E+00	6.0494E-01
11	>	5.6358E+02	9.6090E+01	4.2856E+00	5.8534E-01	N/A	N/A	N/A
	≤	2.9893E+03	−1.8200E+03	1.2860E+02	1.3901E+02	−4.2388E+01	4.2856E+00	5.8534E-01
12	>	6.9462E+00	−5.0711E+00	3.9998E+00	7.4816E-01	N/A	N/A	N/A
	≤	2.8156E+03	−1.7423E+03	1.5070E+02	1.1666E+02	−3.6194E+01	3.9998E+00	7.4816E-01
13	>	−2.1084E+01	1.4860E+01	3.1335E+00	6.5332E-01	N/A	N/A	N/A
	≤	1.0819E+04	−9.4121E+03	3.0134E+03	−3.9954E+02	7.0200E+00	3.1335E+00	6.5332E-01
14	>	−2.1149E+01	1.4525E+01	2.9039E+00	6.4174E-01	N/A	N/A	N/A
	≤	9.8516E+03	−8.8098E+03	2.9341E+03	−4.1703E+02	1.1909E+01	2.9039E+00	6.4174E-01
15	>	−1.8777E+01	−1.7217E+01	3.0210E+00	7.2190E-01	N/A	N/A	N/A
	≤	2.0491E+03	−1.9580E+03	6.5584E+02	−6.7331E+01	−1.0441E+01	3.0210E+00	7.2190E-01
16	>	4.3320E+01	−2.6790E+01	2.3061E+00	7.1970E-01	N/A	N/A	N/A
	≤	−5.3063E+03	4.3833E+03	−1.3472E+03	1.9841E+02	−1.9583E+01	2.3061E+00	7.1970E-01
Band	20 μm	$\bar{g}$ polynomial fitting coefficients (c_i) THM ice cloud						
		$i=1$	$i=2$	$i=3$	$i=4$	$i=5$	$i=6$	$i=7$
1	>	−2.0041E+01	−1.3505E+01	−7.0661E+00	6.4388E-01	N/A	N/A	N/A
	≤	−7.5718E+03	6.6203E+03	−2.0859E+03	2.3356E+02	1.6953E+01	−7.0661E+00	6.4388E-01
2	>	−4.4300E+03	−1.8035E+02	−2.3656E+00	7.8246E-01	N/A	N/A	N/A
	≤	5.7346E+03	−4.2887E+03	9.1710E+02	1.6268E+01	−1.7578E+01	−2.3656E+00	7.8246E-01
3	>	3.6033E+01	4.2182E+01	−1.3877E+00	8.0630E-01	N/A	N/A	N/A
	≤	−5.6572E+02	1.9059E+02	−4.2673E+01	5.1658E+01	−1.4658E+01	−1.3877E+00	8.0630E-01
4	>	2.9815E+02	2.6552E+01	−1.8560E+00	8.4110E-01	N/A	N/A	N/A
	≤	1.1682E+03	−1.2729E+03	5.1127E+02	−7.6580E+01	1.3438E+00	−1.8560E+00	8.4110E-01
5	>	−6.3294E-01	−7.0389E+00	−1.8128E+00	8.8168E-01	N/A	N/A	N/A
	≤	2.3212E+02	−4.1929E+02	2.1313E+02	−2.9723E+01	−1.4856E+00	−1.8128E+00	8.8168E-01
6	>	−7.3294E+00	−6.7420E+00	−1.4179E+00	9.2192E-01	N/A	N/A	N/A
	≤	−5.0281E+02	2.2176E+02	−1.5860E+00	7.2275E+00	−5.9310E+00	−1.4179E+00	9.2192E-01
7	>	−1.4769E+00	1.1304E+01	−7.1090E-01	9.2590E-01	N/A	N/A	N/A
	≤	−1.0152E+03	9.9445E+02	−3.6812E+02	7.3736E+01	−1.0851E+01	−7.1090E-01	9.2590E-01
8	>	−2.5559E+00	3.4942E+01	−6.5364E-02	9.0084E-01	N/A	N/A	N/A
	≤	−9.0384E+02	1.0160E+03	−4.4951E+02	1.0588E+02	−1.5879E+01	−6.5364E-02	9.0084E-01
9	>	2.7340E+02	5.9363E+01	1.2744E-01	8.8427E-01	N/A	N/A	N/A
	≤	7.8318E+02	−4.9504E+02	5.7626E+01	2.7045E+01	−1.0362E+01	1.2744E-01	8.8427E-01
10	>	6.0384E+02	5.7564E+01	−4.7944E-01	8.9304E-01	N/A	N/A	N/A
	≤	4.5351E+03	−3.9449E+03	1.2908E+03	−1.8932E+02	8.9573E+00	−4.7944E-01	8.9304E-01
11	>	2.9571E+02	3.3562E+01	−7.1042E-01	9.0467E-01	N/A	N/A	N/A
	≤	5.3118E+03	−4.7107E+03	1.5927E+03	−2.5020E+02	1.5638E+01	−7.1042E-01	9.0467E-01
12	>	2.6732E+02	6.8483E+01	−4.7094E-01	8.3263E-01	N/A	N/A	N/A
	≤	1.2997E+04	−1.1502E+04	3.8712E+03	−6.0430E+02	3.8720E+01	−4.7094E-01	8.3263E-01
13	>	8.8805E+00	2.5414E+00	−2.4083E+00	8.5994E-01	N/A	N/A	N/A
	≤	1.3022E+04	−1.2300E+04	4.5392E+03	−8.1781E+02	7.0415E+01	−2.4083E+00	8.5994E-01
14	>	−5.6667E-01	−8.4460E+00	−2.6829E+00	8.7048E-01	N/A	N/A	N/A
	≤	1.0222E+04	−1.0031E+04	3.8821E+03	−7.4282E+02	6.9355E+01	−2.6829E+00	8.7048E-01
15	>	−7.8125E+00	8.3205E+00	−2.6929E+00	8.2866E-01	N/A	N/A	N/A
	≤	5.6928E+03	−6.4198E+03	2.8629E+03	−6.2992E+02	6.6879E+01	−2.6929E+00	8.2866E-01
16	>	−1.8371E+01	2.1666E+01	−2.1760E+00	8.1383E-01	N/A	N/A	N/A
	≤	−7.3313E+03	5.4439E+03	−1.2395E+03	2.3739E+01	2.3444E+01	−2.1760E+00	8.1383E-01

Table A3
As in Table A1 but for the MC6 water cloud optical model.

Band	20 μm	$\bar{\kappa}_{ext}$ polynomial fitting coefficients (a_i) for MC6 water cloud						
		$i=1$	$i=2$	$i=3$	$i=4$	$i=5$	$i=6$	$i=7$
1	>	−3.1981E+01	−5.2498E+01	5.2779E-01	1.4601E-01	N/A	N/A	N/A
	≤	−4.3662E+03	4.1356E+03	−1.5361E+03	2.7995E+02	−2.4413E+01	5.2779E-01	1.4601E-01
2	>	−5.4522E+01	−2.5085E+01	2.7016E+00	1.8491E-01	N/A	N/A	N/A
	≤	−2.4662E+03	2.7831E+03	−1.3039E+03	3.2495E+02	−4.4407E+01	2.7016E+00	1.8491E-01
3	>	−5.2025E-01	−9.5381E+00	3.2056E+00	1.8037E-01	N/A	N/A	N/A
	≤	−2.6803E+02	5.2548E+02	−3.8695E+02	1.4641E+02	−3.0714E+01	3.2056E+00	1.8037E-01
4	>	−4.9494E-01	−1.0075E+01	2.9371E+00	1.6907E-01	N/A	N/A	N/A
	≤	−2.6425E+02	4.3271E+02	−2.8920E+02	1.0612E+02	−2.3479E+01	2.9371E+00	1.6907E-01
5	>	−1.9332E+01	−1.5848E+01	2.3300E+00	1.5144E-01	N/A	N/A	N/A
	≤	−6.0375E+02	7.0782E+02	−3.5647E+02	1.0309E+02	−1.9290E+01	2.3300E+00	1.5144E-01
6	>	−3.8676E+01	−3.7696E+01	1.0162E+00	1.3524E-01	N/A	N/A	N/A
	≤	−2.0804E+03	2.0212E+03	−7.8945E+02	1.6010E+02	−1.8036E+01	1.0162E+00	1.3524E-01
7	>	−1.2305E+03	−1.0774E+02	1.4258E+00	1.8593E-01	N/A	N/A	N/A
	≤	−6.9746E+03	6.6372E+03	−2.5028E+03	4.7457E+02	−4.5773E+01	1.4258E+00	1.8593E-01
8	>	−1.3437E+03	−8.4912E+01	3.2964E+00	2.1272E-01	N/A	N/A	N/A
	≤	−1.0410E+04	1.0125E+04	−3.9389E+03	7.8284E+02	−8.1789E+01	3.2964E+00	2.1272E-01
9	>	3.9182E+01	3.2816E+01	5.8398E+00	2.1557E-01	N/A	N/A	N/A
	≤	−7.4591E+03	8.0623E+03	−3.5728E+03	8.3331E+02	−1.0612E+02	5.8398E+00	2.1557E-01
10	>	1.2754E+03	1.2500E+02	7.1991E+00	2.0369E-01	N/A	N/A	N/A
	≤	3.2044E+03	−1.2248E+03	−5.6233E+02	4.0987E+02	−8.9287E+01	7.1991E+00	2.0369E-01
11	>	5.8976E+02	7.9623E+01	6.3046E+00	1.9194E-01	N/A	N/A	N/A
	≤	1.0424E+04	−8.2786E+03	2.1568E+03	−1.0621E+02	−4.3069E+01	6.3046E+00	1.9194E-01
12	>	1.3291E+03	1.1807E+02	6.3270E+00	1.8343E-01	N/A	N/A	N/A
	≤	3.2260E+04	−2.8098E+04	9.0012E+03	−1.1932E+03	2.5787E+01	6.3270E+00	1.8343E-01
13	>	−1.0402E+01	−2.4070E+00	3.6016E+00	1.8191E-01	N/A	N/A	N/A
	≤	3.7023E+04	−3.4640E+04	1.2379E+04	−2.0172E+03	1.1744E+02	3.6016E+00	1.8191E-01
14	>	−1.2718E+03	−8.9530E+01	2.3116E+00	1.8401E-01	N/A	N/A	N/A
	≤	3.1778E+04	−3.1442E+04	1.2045E+04	−2.1522E+03	1.4899E+02	2.3116E+00	1.8401E-01
15	>	−1.8841E+03	−1.3682E+02	1.4857E+00	1.8627E-01	N/A	N/A	N/A
	≤	1.2316E+04	−1.5676E+04	7.5535E+03	−1.6709E+03	1.4429E+02	1.4857E+00	1.8627E-01
16	>	−2.9873E+02	−2.9478E+01	2.9053E+00	1.7886E-01	N/A	N/A	N/A
	≤	−2.4792E+04	1.8773E+04	−4.4961E+03	2.1530E+02	3.1834E+01	2.9053E+00	1.7886E-01
24	>	−1.1906E+01	1.4715E+00	3.2622E+00	1.5791E-01	N/A	N/A	N/A
	≤	6.0147E+02	−3.3763E+02	6.4074E+01	−6.6621E+00	2.0132E+00	3.2622E+00	1.5791E-01
Band	20 μm	$\bar{\omega}$ polynomial fitting coefficients (b_i) for MC6 water cloud						
		$i=1$	$i=2$	$i=3$	$i=4$	$i=5$	$i=6$	$i=7$
1	>	−1.9137E+03	−9.4255E+01	−3.5182E+00	3.8188E-01	N/A	N/A	N/A
	≤	−2.5595E+03	2.5729E+03	−9.7865E+02	1.5366E+02	8.5947E-01	−3.5182E+00	3.8188E-01
2	>	−1.2696E+03	−5.5470E+01	−1.9522E+00	4.4321E-01	N/A	N/A	N/A
	≤	−1.6684E+03	1.6595E+03	−6.8567E+02	1.4512E+02	−1.1072E+01	−1.9522E+00	4.4321E-01
3	>	−3.0119E+02	−1.9329E+00	−1.8314E+00	4.3340E-01	N/A	N/A	N/A
	≤	−1.8012E+03	1.6548E+03	−6.0440E+02	1.0990E+02	−6.7073E+00	−1.8314E+00	4.3340E-01
4	>	−7.5383E+00	8.5664E+00	−2.1245E+00	4.2307E-01	N/A	N/A	N/A
	≤	−1.6060E+03	1.4510E+03	−5.0150E+02	7.8262E+01	−1.4044E+00	−2.1245E+00	4.2307E-01
5	>	−1.0488E+01	4.1583E+00	−2.5591E+00	4.0326E-01	N/A	N/A	N/A
	≤	−1.3223E+03	1.1577E+03	−3.6608E+02	4.0665E+01	4.9184E+00	−2.5591E+00	4.0326E-01
6	>	−1.2339E+03	−1.0233E+02	−2.8383E+00	4.7700E-01	N/A	N/A	N/A
	≤	−2.6434E+03	2.4352E+03	−8.4732E+02	1.2608E+02	−9.2968E-01	−2.8383E+00	4.7700E-01
7	>	−4.8062E+03	−3.1169E+02	−1.6947E-02	7.0447E-01	N/A	N/A	N/A
	≤	−4.9194E+03	4.6872E+03	−1.7880E+03	3.5173E+02	−3.6168E+01	−1.6947E-02	7.0447E-01
8	>	−5.2282E+03	−3.1693E+02	1.5545E+00	7.5117E-01	N/A	N/A	N/A
	≤	−7.2838E+03	6.8316E+03	−2.5473E+03	4.8851E+02	−5.1819E+01	1.5545E+00	7.5117E-01
9	>	−4.3154E+03	−2.3471E+02	3.2803E+00	7.4964E-01	N/A	N/A	N/A
	≤	−1.0229E+04	9.6251E+03	−3.5926E+03	6.8592E+02	−7.2823E+01	3.2803E+00	7.4964E-01
10	>	−2.7335E+03	−1.1042E+02	4.8594E+00	7.1621E-01	N/A	N/A	N/A
	≤	−1.2297E+04	1.1705E+04	−4.4338E+03	8.6170E+02	−9.3369E+01	4.8594E+00	7.1621E-01
11	>	−2.7837E+02	3.6919E+01	4.8195E+00	6.4293E-01	N/A	N/A	N/A
	≤	−8.3323E+03	8.2689E+03	−3.3150E+03	6.9702E+02	−8.3843E+01	4.8195E+00	6.4293E-01
12	>	−3.8083E+01	−3.9982E+01	4.3230E+00	8.1750E-01	N/A	N/A	N/A
	≤	−7.6101E+03	7.5075E+03	−2.9768E+03	6.1169E+02	−7.0509E+01	4.3230E+00	8.1750E-01
13	>	−1.0894E+01	2.4505E+00	4.8331E+00	7.4888E-01	N/A	N/A	N/A
	≤	5.1836E+01	9.3781E+02	−8.7686E+02	3.1363E+02	−5.5567E+01	4.8331E+00	7.4888E-01
14	>	3.5230E+01	−4.8590E+01	3.5177E+00	8.0978E-01	N/A	N/A	N/A
	≤	2.3949E+03	−1.4028E+03	6.1186E+01	1.1980E+02	−3.3321E+01	3.5177E+00	8.0978E-01
15	>	2.5481E+03	1.9397E+01	2.1668E+00	8.7078E-01	N/A	N/A	N/A
	≤	2.9969E+03	−2.2684E+03	5.3392E+02	−8.2064E+00	−1.4759E+01	2.1668E+00	8.7078E-01
16	>	1.2006E+03	−2.6485E+01	1.2298E+00	7.9274E-01	N/A	N/A	N/A
	≤	4.3545E+03	−4.2144E+03	1.5523E+03	−2.5644E+02	1.2946E+01	1.2298E+00	7.9274E-01
Band	20 μm	$\bar{g}$ polynomial fitting coefficients (c_i) for MC6 water cloud						
		$i=1$	$i=2$	$i=3$	$i=4$	$i=5$	$i=6$	$i=7$

(continued on next page)

Table A3 (*continued*)

1	>	8.9995E+00	9.0259E-01	−6.9317E+00	5.8329E-01	N/A	N/A	N/A
	≤	−7.3621E+03	6.4120E+03	−1.9867E+03	2.0660E+02	2.0164E+01	−6.9317E+00	5.8329E-01
2	>	1.8283E+01	−1.5760E+01	−4.5137E+00	7.5315E-01	N/A	N/A	N/A
	≤	−5.4924E+03	5.8976E+03	−2.4685E+03	4.7587E+02	−2.7977E+01	−4.5137E+00	7.5315E-01
3	>	1.8766E+01	−1.4218E+01	−3.2042E+00	8.1728E-01	N/A	N/A	N/A
	≤	2.0409E+03	−7.9557E+02	−2.9819E+02	1.9233E+02	−2.3121E+01	−3.2042E+00	8.1728E-01
4	>	1.8613E+01	−1.4745E+01	−2.6872E+00	8.5347E-01	N/A	N/A	N/A
	≤	4.6588E+03	−3.5318E+03	7.7787E+02	8.2161E+00	−1.3861E+01	−2.6872E+00	8.5347E-01
5	>	1.8545E+01	−1.4963E+01	−2.3921E+00	8.8352E-01	N/A	N/A	N/A
	≤	4.5753E+03	−3.8663E+03	1.0734E+03	−7.0774E+01	−8.0699E+00	−2.3921E+00	8.8352E-01
6	>	−2.0196E+01	−1.2721E+01	−1.8639E+00	9.2090E-01	N/A	N/A	N/A
	≤	3.4520E+02	−7.5716E+02	3.6327E+02	−3.5840E+01	−5.9163E+00	−1.8639E+00	9.2090E-01
7	>	−1.0051E+01	5.2525E+00	−1.1252E+00	9.1554E-01	N/A	N/A	N/A
	≤	−3.1923E+03	2.5926E+03	−7.7221E+02	1.2103E+02	−1.4223E+01	−1.1252E+00	9.1554E-01
8	>	−1.9025E+01	2.0549E+01	−5.8942E-01	9.0383E-01	N/A	N/A	N/A
	≤	−2.6383E+03	2.4580E+03	−8.6765E+02	1.5743E+02	−1.8444E+01	−5.8942E-01	9.0383E-01
9	>	5.9495E+02	6.9397E+01	3.4060E-02	8.8667E-01	N/A	N/A	N/A
	≤	−1.5889E+03	1.7241E+03	−7.2846E+02	1.5894E+02	−2.1102E+01	3.4060E-02	8.8667E-01
10	>	1.9420E+03	1.4676E+02	4.5821E-01	8.7217E-01	N/A	N/A	N/A
	≤	−6.7311E+02	9.2011E+02	−4.8487E+02	1.3065E+02	−2.0750E+01	4.5821E-01	8.7217E-01
11	>	1.2345E+03	9.7963E+01	3.9543E-02	8.8766E-01	N/A	N/A	N/A
	≤	1.2991E+03	−9.7470E+02	2.2588E+02	−1.3622E+00	−7.9700E+00	3.9543E-02	8.8766E-01
12	>	2.6295E+03	2.1929E+02	1.2934E+00	8.2220E-01	N/A	N/A	N/A
	≤	4.1223E+03	−3.2628E+03	8.7399E+02	−6.4499E+01	−1.0893E+01	1.2934E+00	8.2220E-01
13	>	2.3474E+03	1.6331E+02	−6.1451E-01	8.2576E-01	N/A	N/A	N/A
	≤	1.5908E+04	−1.4008E+04	4.6776E+03	−7.2180E+02	4.5624E+01	−6.1451E-01	8.2576E-01
14	>	5.9599E+02	6.5846E+01	−1.6318E+00	8.1162E-01	N/A	N/A	N/A
	≤	2.2391E+04	−2.0034E+04	6.8579E+03	−1.1067E+03	7.8921E+01	−1.6318E+00	8.1162E-01
15	>	−6.2969E+02	−2.3774E+01	−3.1533E+00	8.0337E-01	N/A	N/A	N/A
	≤	2.5428E+04	−2.3419E+04	8.3474E+03	−1.4315E+03	1.1448E+02	−3.1533E+00	8.0337E-01
16	>	−1.2448E+03	−8.4963E+01	−3.9177E+00	8.3317E-01	N/A	N/A	N/A
	≤	4.8714E+03	−6.2083E+03	3.0527E+03	−7.2863E+02	8.3963E+01	−3.9177E+00	8.3317E-01

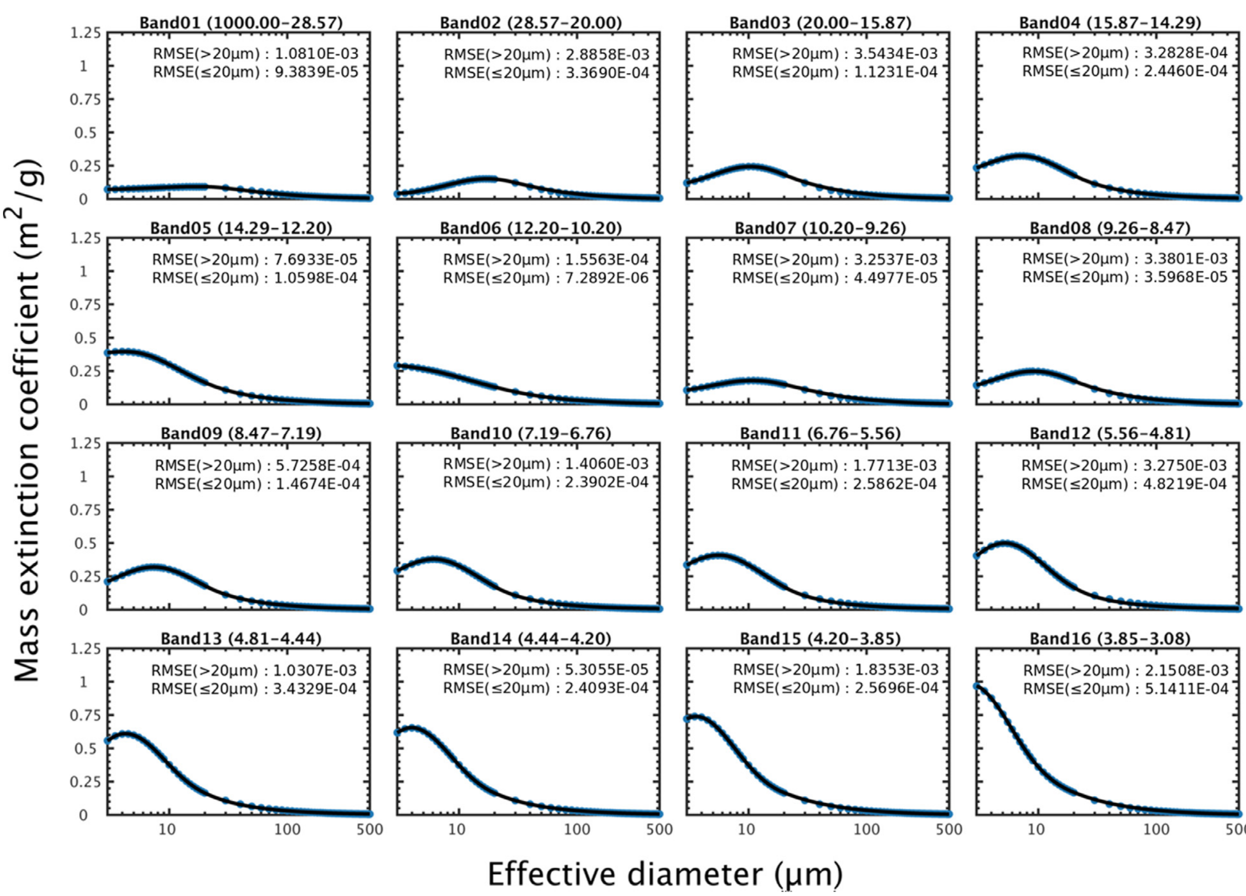

Fig. A1. Parameterizations of $\bar{\kappa}_{ext}$ in 16 RRTMG_LW bands for the MC6 ice cloud optical model. Blue dots are discrete vales of $\bar{\kappa}_{ext}$, and black lines are fitted curves, for each RRTMG_LW spectral band. Numbers in parentheses in sub-titles are the spectral ranges for each band in wavelength (µm). RMSE(> 20 µm) and RMSE(≤ 20 µm) in sub-figures are the root-mean-square errors for D_e > and ≤ 20 µm, respectively.

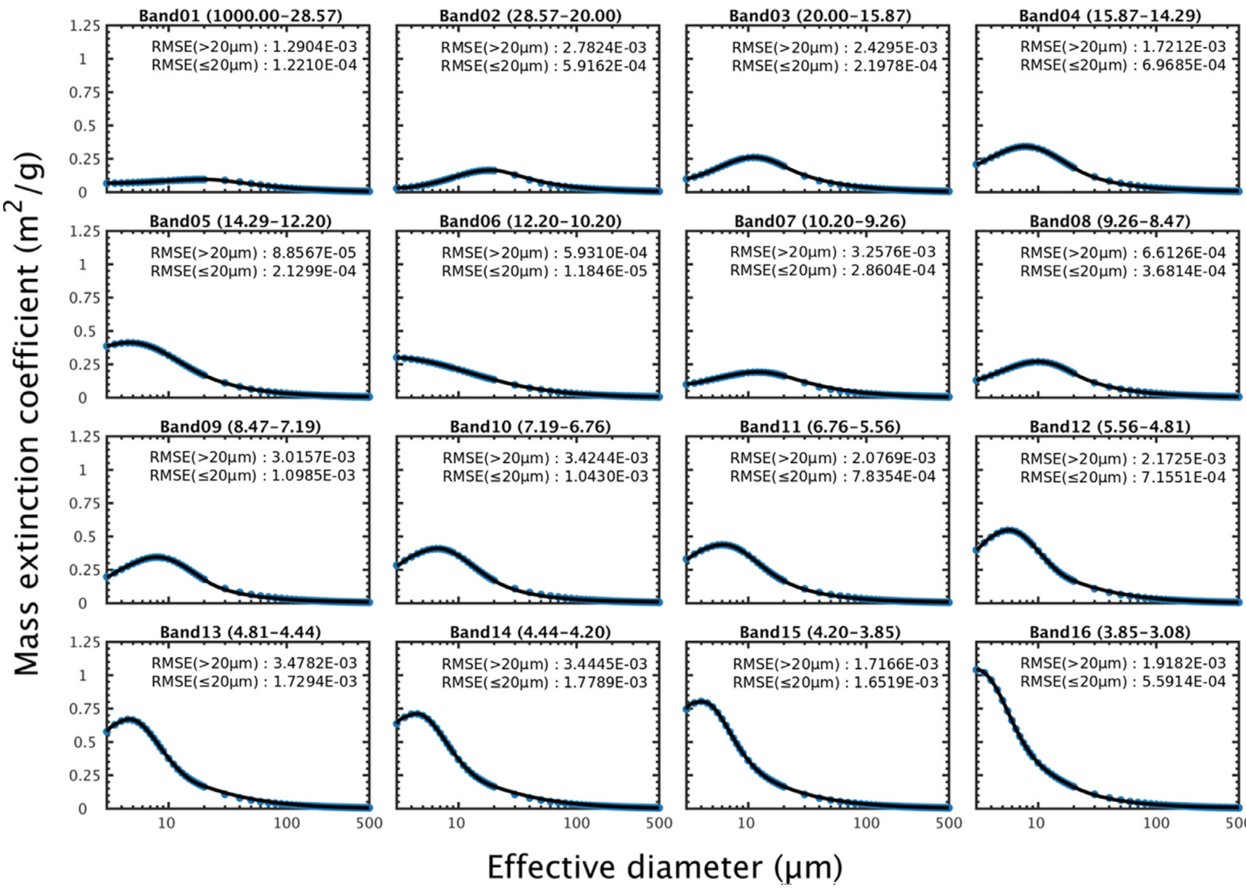

Fig. A2. Same as Fig. A1 except for the THM ice cloud optical model.

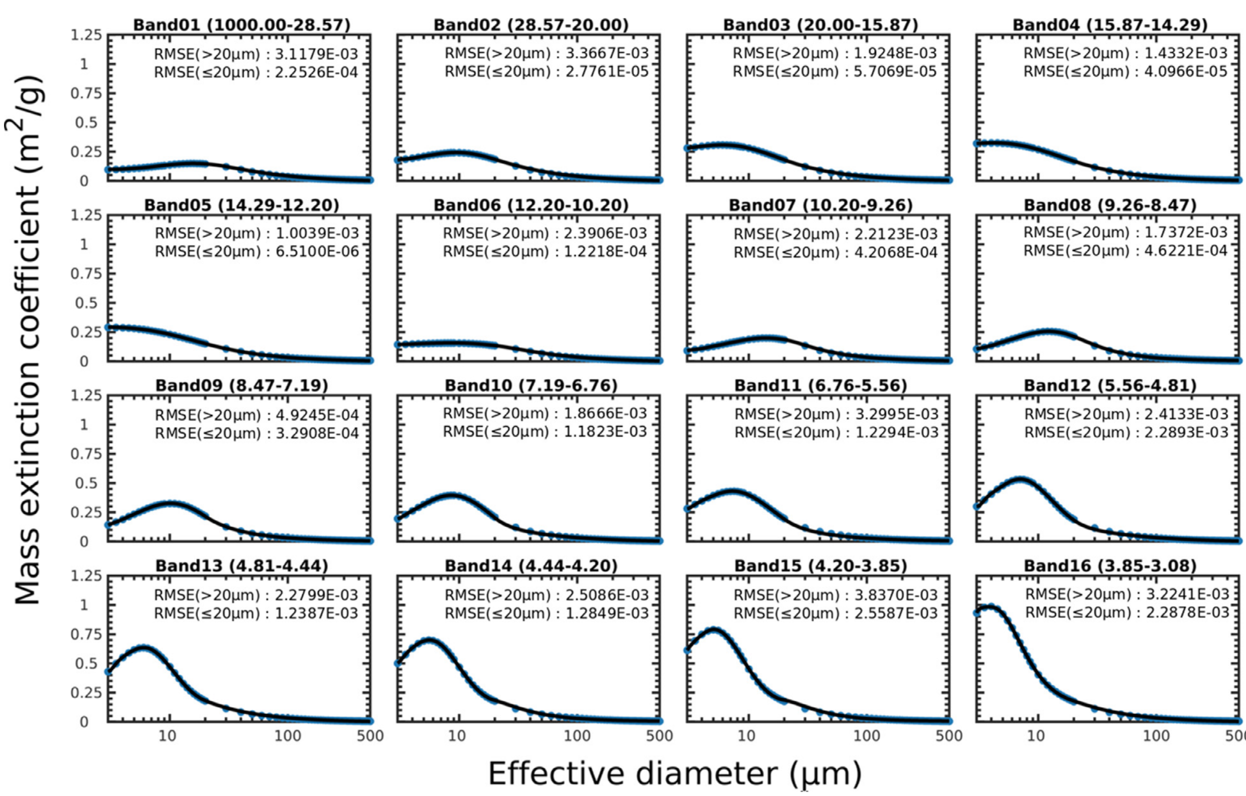

Fig. A3. Same as Fig. A1 except for the MC6 water cloud optical model.

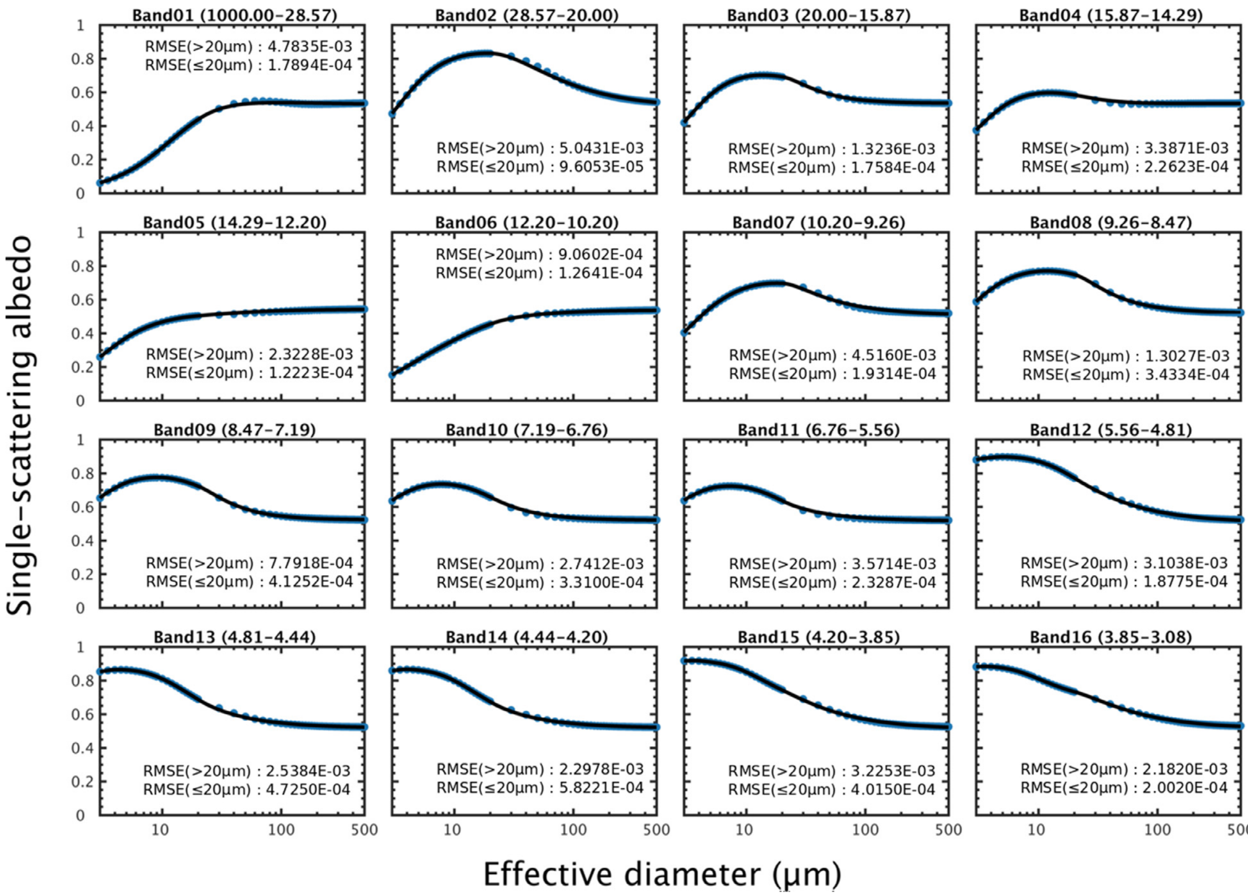

Fig. A4. Parameterizations of $\bar{\omega}$ in 16 RRTMG_LW bands for the MC6 ice cloud optical model. Blue dots are discrete vales of $\bar{\omega}$, and black lines are fitted curves, for each RRTMG_LW spectral band. Numbers in parentheses in sub-titles are the spectral ranges for each band in wavelength (μm). RMSE($>$ 20 μm) and RMSE($\leq$ 20 μm) in sub-figures are the root-mean-square errors for D_e $>$ and $\leq$ 20 μm, respectively.

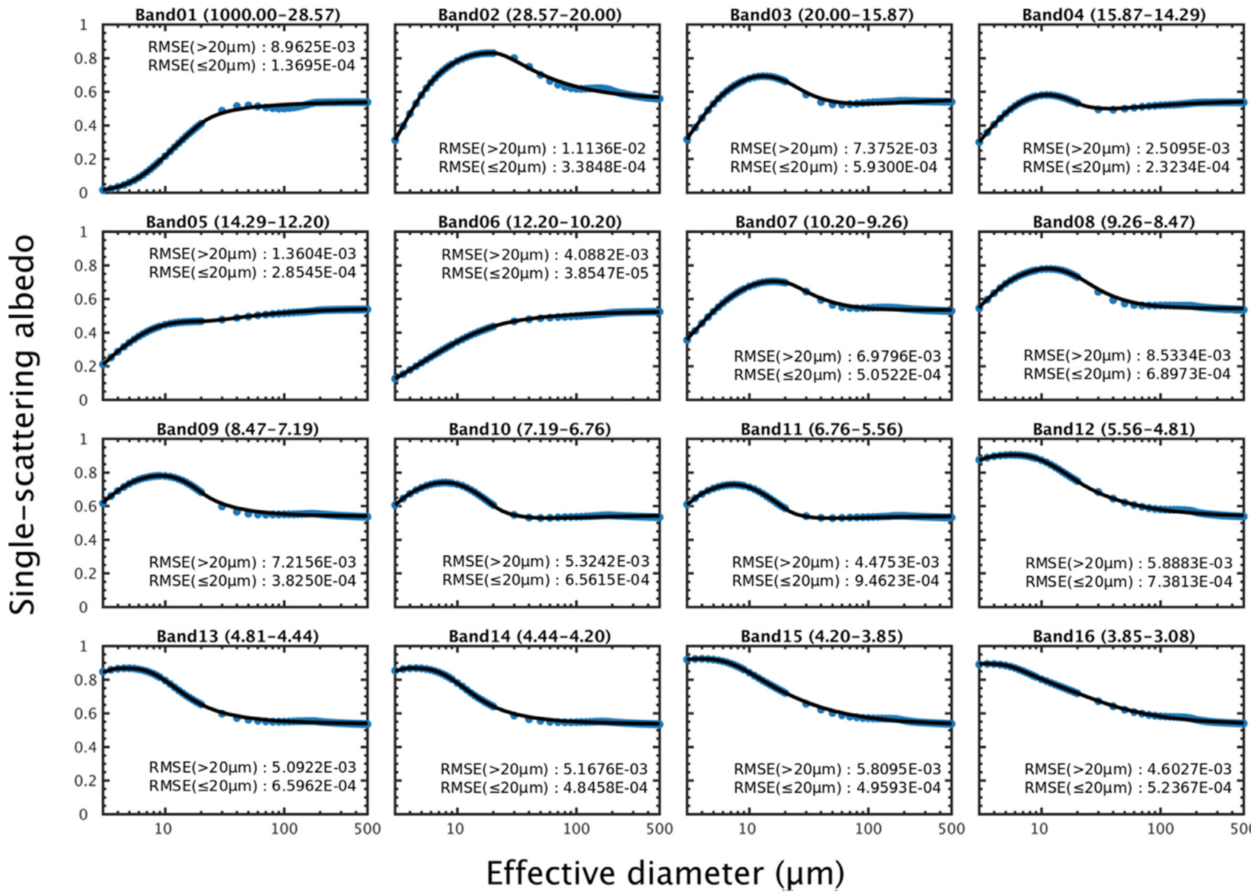

Fig. A5. Same as Fig. A4 except for the THM ice cloud optical model.

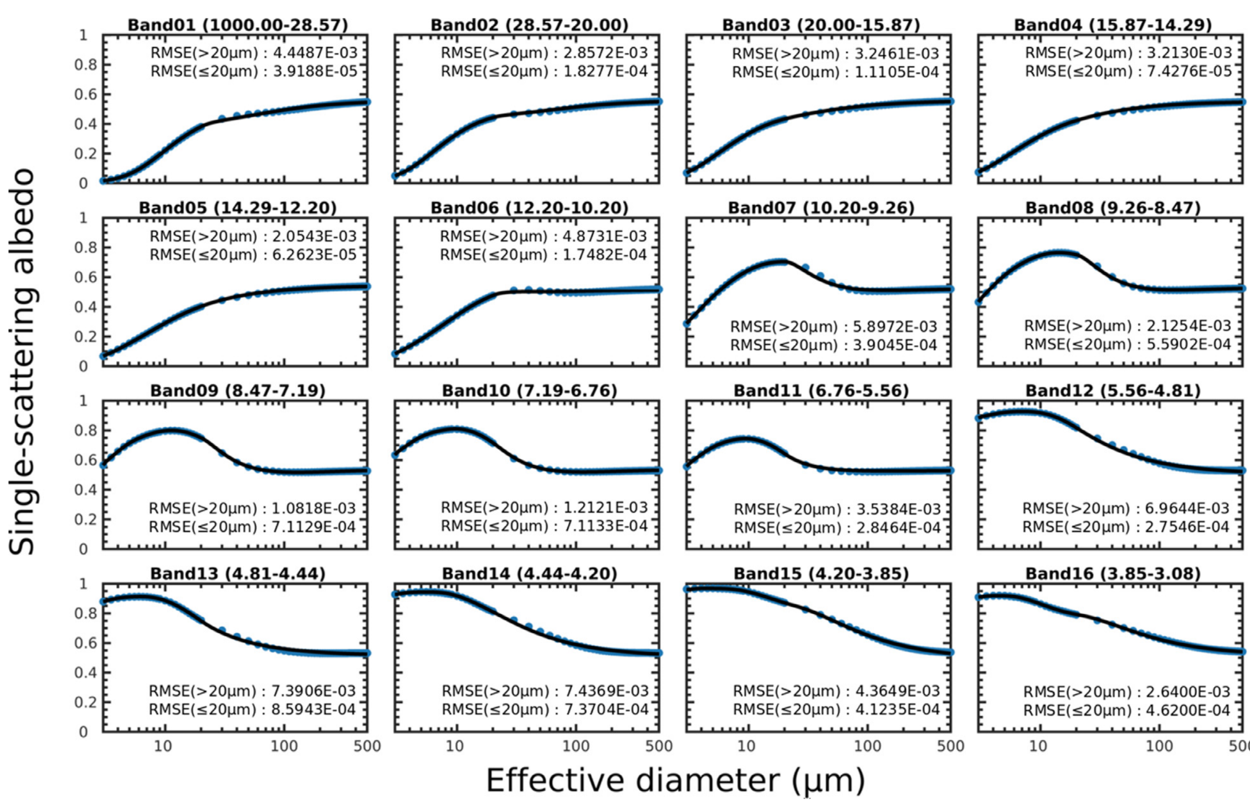

Fig. A6. Same as Fig. A4 except for the MC6 water cloud optical model.

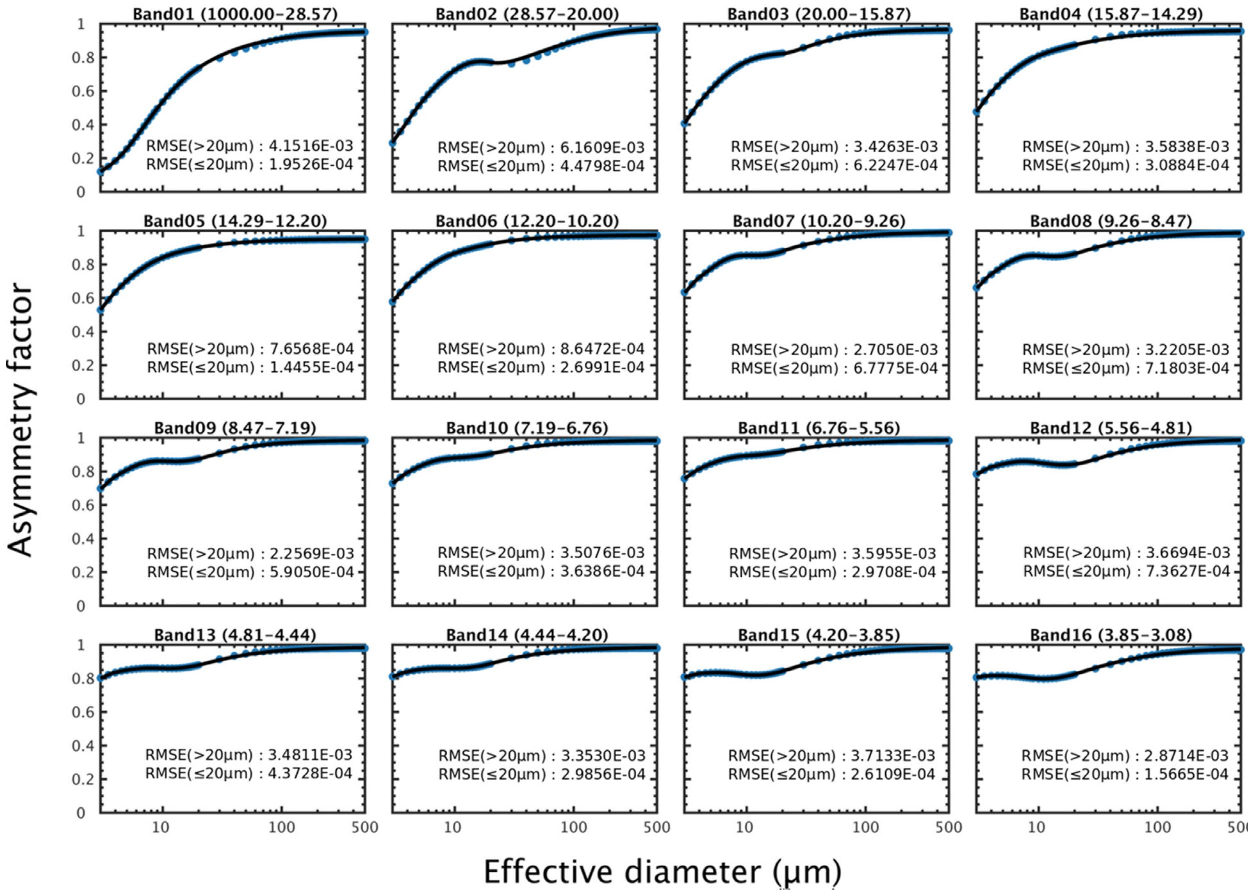

Fig. A7. Parameterizations of $\bar{g}$ in 16 RRTMG_LW bands for the MC6 ice cloud optical property model. Blue dots are discrete vales of $\bar{g}$, and black lines are fitted curves, for each RRTMG_LW spectral band. Numbers in parentheses in sub-titles are the spectral ranges for each band in wavelength (μm). RMSE($>$ 20 μm) and RMSE($\leq$ 20 μm) in sub-figures are the root-mean-square errors for $D_e >$ and $\leq$ 20 μm, respectively.

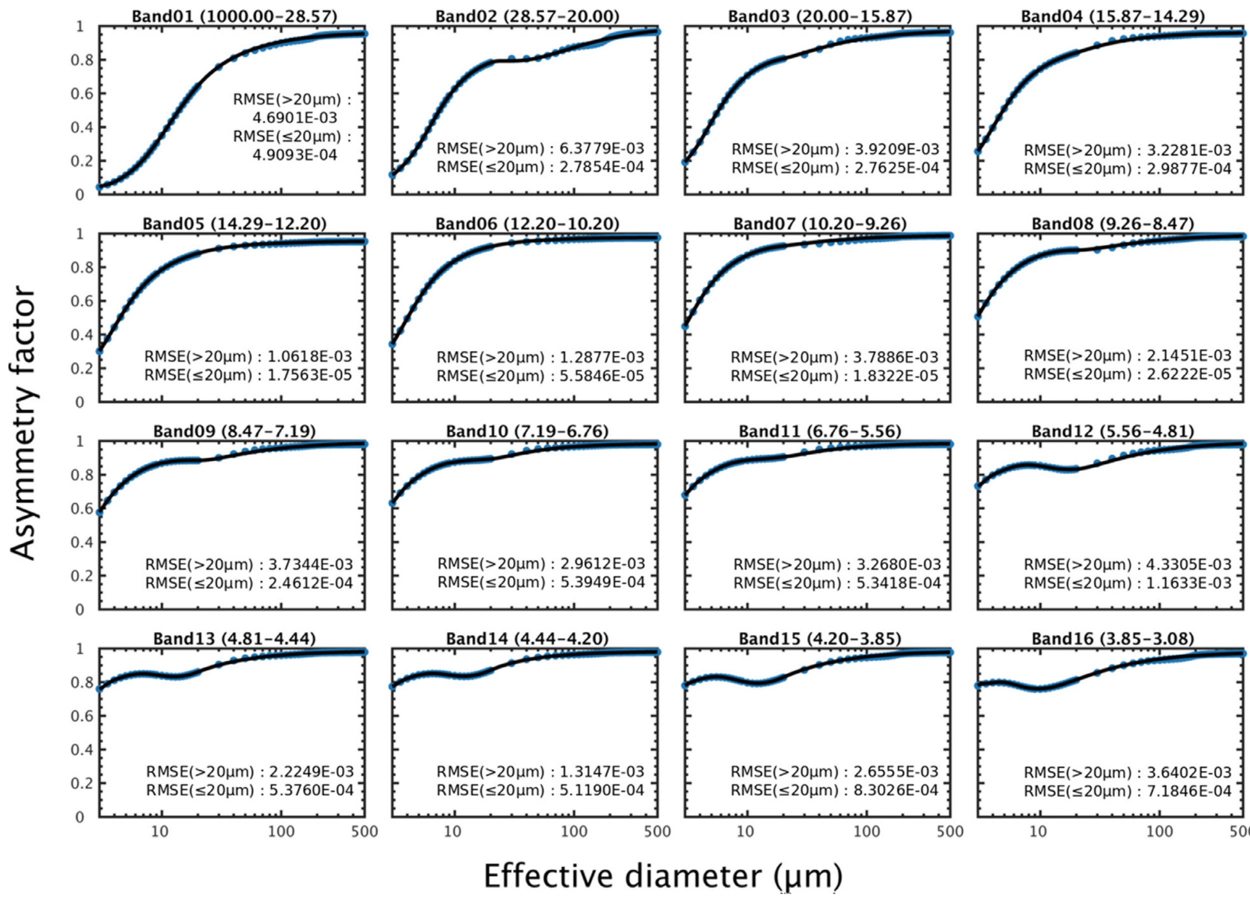

Fig. A8. Same as Fig. A7 except for the THM ice cloud optical property model.

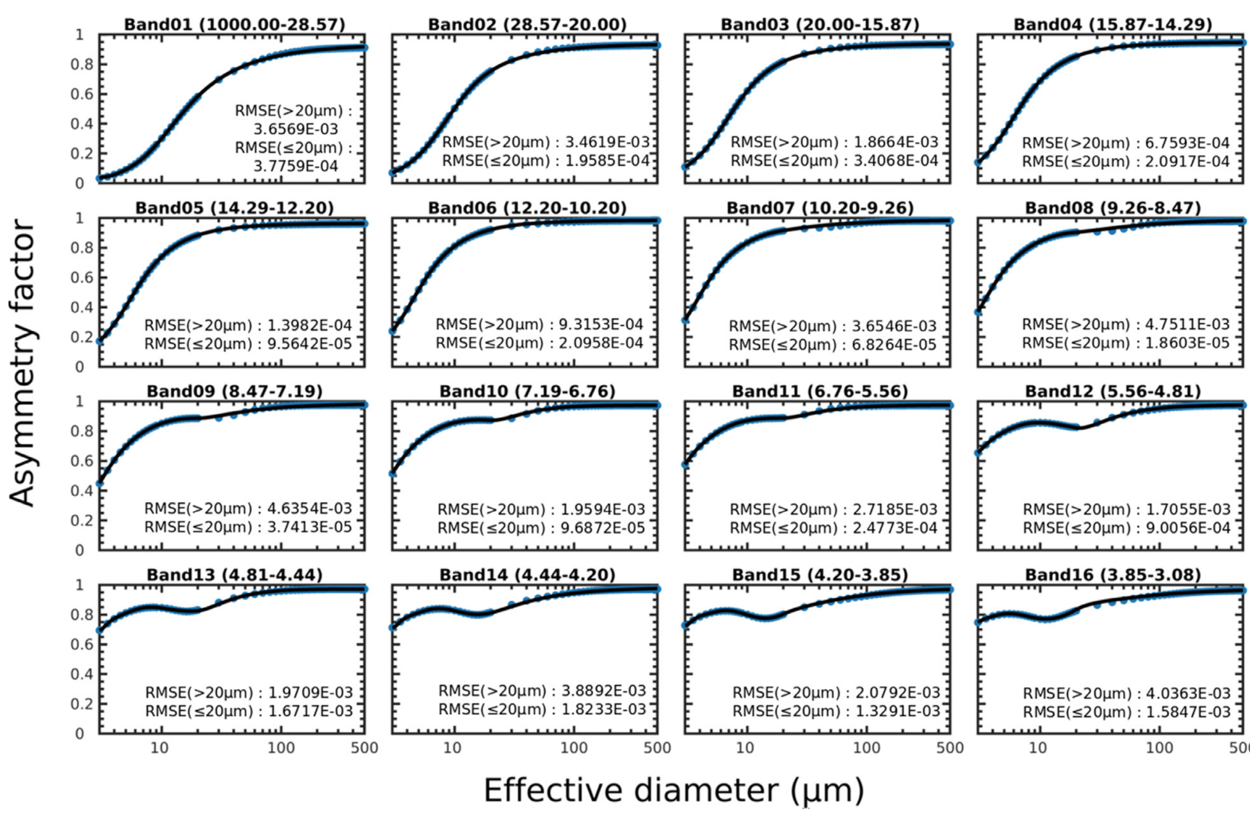

Fig. A9. Same as Fig. A7 except for the MC6 water cloud optical property model.

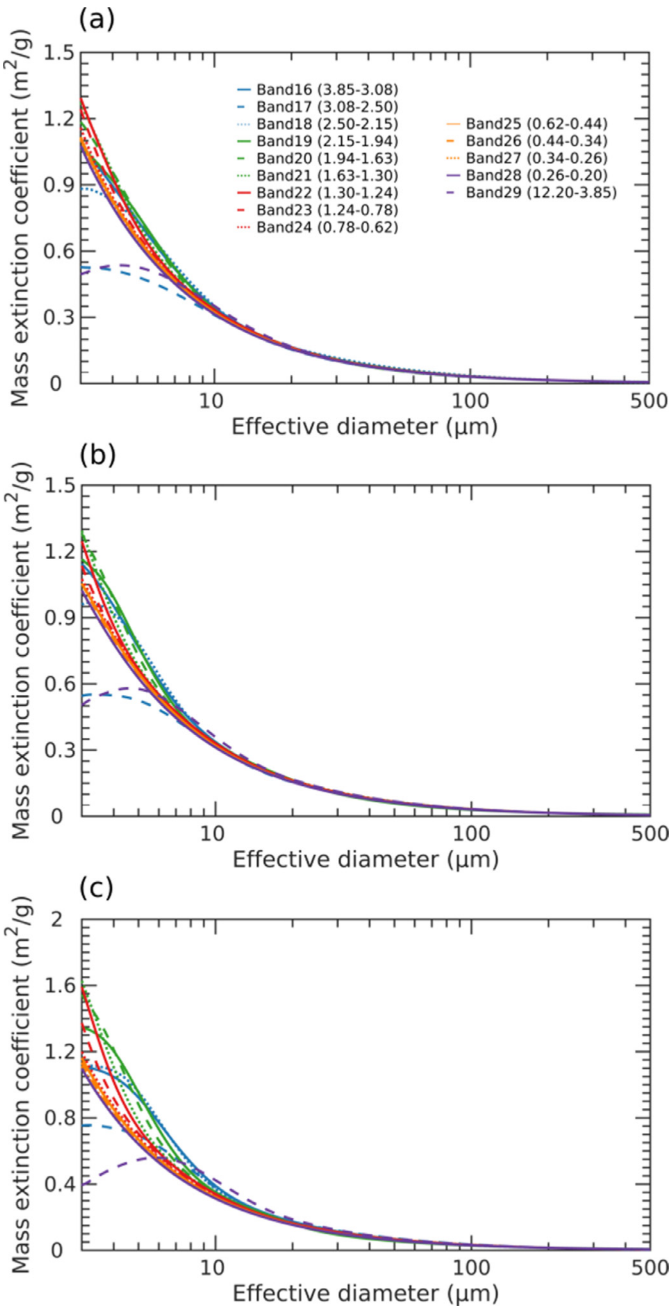

Fig. A10. Parameterized $\bar{\kappa}_{ext}$ (m^2/g) as a function of D_e in the 14 RRTMG_SW spectral bands for (a) MC6 ice, (b) THM ice, and (c) MC6 water cloud models. Numbers in parentheses are the spectral ranges for the bands in the wavelength domain.

References

[1] von Salzen K, Scinocca JF, McFarlane NA, Li J, Cole JNS, Plummer D, et al. The Canadian fourth generation atmospheric global climate model (CanAM4). part I: representation of physical processes. Atmos-Ocean 2013;51:104–25. doi:10.1080/07055900.2012.755610.

[2] Li J. Accounting for unresolved clouds in a 1D infrared radiative transfer model. Part I: solution for radiative transfer, including cloud scattering and overlap. J Atmos Sci 2002;59:3302–20 doi:10.1175/1520-0469(2002)059<3302:AFUCIA>2.0.CO;2.

[3] Neale R.B., Richter J.H., Conley A.J., Park S., Lauritzen P.H., Gettelman A., et al. Description of the NCAR community atmosphere model (CAM 4.0), https://www.cesm.ucar.edu/models/ccsm4.0/cam/docs/description/cam4_desc.pdf. NCAR Technical Note NCAR/TN-485+STR 2010 [accessed 2 August 2019].

[4] Ramanathan V, Downey P. A nonisothermal emissivity and absorptivity formulation for water vapor. J Geophys Res 1986;91:8649–66. doi:10.1029/JD091iD08p08649.

[5] Neale R.B., Gettelman A., Park S., Chen C., Lauritzen P.H., Williamson D.L., et al. Description of the NCAR community atmosphere model (CAM 5.0), http://www.cesm.ucar.edu/models/cesm1.0/cam/docs/description/cam5_desc.pdf. NCAR Technical Note NCAR/TN-486+STR 2012 [accessed 2 August 2019].

[6] CAM6 User's Guide, https://ncar.github.io/CAM/doc/build/html/users_guide/; [accessed 2 August 2019].

[7] Clough SA, Shephard MW, Mlawer EJ, Delamere JS, Iacono MJ, Cady-Pereira K, et al. Atmospheric radiative transfer modeling: a summary of the aer codes. J Quant Spectrosc Radiat Transf 2005;91:233–44. doi:10.1016/j.jqsrt.2004.05.058.

[8] Iacono MJ, Delamere JS, Mlawer EJ, Shephard MW, Clough SA, Collins WD. Radiative forcing by long-lived greenhouse gases: ccalculations with the aer radiative transfer models. J Geophys Res 2008;113:D13103. doi:10.1029/2008JD009944.

[9] Mlawer EJ, Taubman SJ, Brown PD, Iacono MJ, Clough SA. Radiative transfer for inhomogeneous atmospheres: RRTM, a validated correlated-k model for the longwave. J Geophys Res 1997;102:16663–82. doi:10.1029/97JD00237.

[10] Mlawer EJ, Iacono MJ, Pincus R, Barker HW, Oreopoulos L, Mitchell DL. Contributions of the arm program to radiative transfer modeling for climate and weather applications. Meteorol Monogr 2016;57:15 1-15.19. doi:10.1175/AMSMONOGRAPHS-D-15-0041.1.

[11] Saha S, Moorthi S, Pan H-L, Wu X, Wang J, Nadiga S, et al. The NCEP climate forecast system reanalysis. Bull Am Meteorol Soc 2010;91:1015–58. doi:10.1175/2010BAMS3001.1.

[12] Saha S, Moorthi S, Wu X, Wang J, Nadiga S, Tripp P, et al. The NCEP climate forecast system version 2. J Clim 2014;27:2185–208. doi:10.1175/JCLI-D-12-00823.1.

[13] Roeckner E., Bäuml G., Bonaventura L., Brokopf R., Esch M., Giorgetta M., et al. The atmospheric general circulation model ECHAM 5. Part I: mmodel description, http://www.mpimet.mpg.de/fileadmin/publikationen/Reports/max_scirep_349.pdf; MPI-Report No. 349 2003 [accessed 2 August 2019].

[14] Stevens B, Giorgetta M, Esch M, Mauritsen T, Crueger T, Rast S, et al. Atmospheric component of the MPI-M earth system model: ECHAM6. J Adv Model Earth Syst 2013;5:146–72. doi:10.1002/jame.20015.

[15] Pope VD, Gallani ML, Rowntree PR, Stratton RA. The impact of new physical parametrizations in the Hadley Centre climate model: hadAM3. Clim Dyn 2000;16:123–46. doi:10.1007/s003820050009.

[16] Cusack S, Edwards JM, Crowther JM. Investigating K distribution methods for parameterizing gaseous absorption in the Hadley Centre climate model. J Geophys Res Atmos 1999;104:2051–7. doi:10.1029/1998JD200063.

[17] Edwards JM, Slingo A. Studies with a flexible new radiation code. I: choosing a configuration for a large-scale model. Q J R Meteorol Soc 1996;122:689–719. doi:10.1002/qj.49712253107.

[18] Goody RM, Yung YL. Atmospheric radiation: theoretical basis. 2nd ed. New York: Oxford University Press; 1989.

[19] Zdunkowski WG, Panhans W-G, Welch RM, Korb GJ. A radiation scheme for circulation and climate models. Contrib Atmos Phys 1982;55:215–38.

[20] Hourdin F, Musat I, Bony S, Braconnot P, Codron F, Dufresne J-L, et al. The LMDZ4 general circulation model: climate performance and sensitivity to parametrized physics with emphasis on tropical convection. Clim Dyn 2006;27:787–813. doi:10.1007/s00382-006-0158-0.

[21] Morcrette J-J. Radiation and cloud radiative properties in the European centre for medium range weather forecasts forecasting system. J Geophys Res 1991;96:9121–32. doi:10.1029/89JD01597.

[22] Fita L. LMDZ physical schemes. A brief description for the LMDZ-B configuration, http://lmdz.lmd.jussieu.fr/developpeurs/notes-techniques/ressources/LMDZphys.pdf; 2013 [accessed 2 August 2019].

[23] Hourdin F, Foujols M-A, Codron F, Guemas V, Dufresne J-L, Bony S, et al. Impact of the LMDZ atmospheric grid configuration on the climate and sensitivity of the IPSL-CM5A coupled model. Clim Dyn 2013;40:2167–92. doi:10.1007/s00382-012-1411-3.

[24] Anderson JL, Balaji V, Broccoli AJ, Cooke WF, Delworth TL, Dixon KW, et al. The new GFDL global atmosphere and land model AM2–LM2: evaluation with prescribed SST simulations. J Clim 2004;17:4641–73. doi:10.1175/JCLI-3223.1.

[25] Donner LJ, Wyman BL, Hemler RS, Horowitz LW, Ming Y, Zhao M, et al. The dynamical core, physical parameterizations, and basic simulation characteristics of the atmospheric component AM3 of the GFDL global coupled model CM3. J Clim 2011;24:3484–519. doi:10.1175/2011JCLI3955.1.

[26] Schwarzkopf MD, Ramaswamy V. Radiative effects of CH4, N2O, halocarbons and the foreign-broadened H2O continuum: aa GCM experiment. J Geophys Res Atmos 1999;104:9467–88. doi:10.1029/1999JD900003.

[27] Ramachandran S, Ramaswamy V, Stenchikov GL, Robock A. Radiative impact of the mount pinatubo volcanic eruption: llower stratospheric response. J Geophys Res Atmos 2000;105:24409–29. doi:10.1029/2000JD900355.

[28] Schmidt GA, Ruedy R, Hansen JE, Aleinov I, Bell N, Bauer M, et al. Present-day atmospheric simulations using GISS model E: comparison to in situ, satellite, and reanalysis data. J Clim 2006;19:153–92. doi:10.1175/JCLI3612.1.

[29] Schmidt GA, Kelley M, Nazarenko L, Ruedy R, Russell GL, Aleinov I, et al. Configuration and assessment of the GISS modelE2 contributions to the CMIP5 archive. J Adv Model Earth Syst 2014;6:141–84. doi:10.1002/2013MS000265.

[30] Hansen J, Russell G, Rind D, Stone P, Lacis A, Lebedeff S, et al. Efficient three-dimensional global models for climate studies: mmodels I and II. Mon Weather Rev 1983;111:609–62 10.1175/1520-0493(1983)111<0609:ETDGMF>2.0.CO;2.

[31] Stephens GL. The parameterization of radiation for numerical weather prediction and climate models. Mon Weather Rev 1984;112:826–67 doi:10.1175/1520-0493(1984)112<0826:TPORFN>2.0.CO;2.

[32] Fu Q, Liou KN, Cribb MC, Charlock TP, Grossman A. Multiple scattering parameterization in thermal infrared radiative transfer. J Atmos Sci 1997;54:2799–812 doi:10.1175/1520-0469(1997)054<2799:MSPITI>2.0.CO;2.
[33] Kuo C-P, Yang P, Huang XL, Feldman D, Flanner M, Kuo C, et al. Impact of multiple scattering on longwave radiative transfer involving clouds. J Adv Model Earth Syst 2017;9:3082–98. doi:10.1002/2017MS001117.
[34] Tang G, Yang P, Kattawar GW, Huang X, Mlawer EJ, Baum BA, et al. Improvement of the simulation of cloud longwave scattering in broadband radiative transfer models. J Atmos Sci 2018;75:2217–33. doi:10.1175/JAS-D-18-0014.1.
[35] Zhao W, Peng Y, Wang B, Li J. Cloud longwave scattering effect and its impact on climate simulation. Atmosphere (Basel) 2018;9:153. doi:10.3390/atmos9040153.
[36] Ritter B, Geleyn J-F. A comprehensive radiation scheme for numerical weather prediction models with potential applications in climate simulations. Mon Weather Rev 1992;120:303–25 10.1175/1520-0493(1992)120<0303:ACRSFN>2.0.CO;2.
[37] Joseph E, Min Q. Assessment of multiple scattering and horizontal inhomogeneity in ir radiative transfer calculations of observed thin cirrus clouds. J Geophys Res 2003;108:4380. doi:10.1029/2002JD002831.
[38] Costa SMS, Shine KP. An estimate of the global impact of multiple scattering by clouds on outgoing long-wave radiation. Q J R Meteorol Soc 2006;132:885–95. doi:10.1256/qj.05.169.
[39] Stephens GL, Gabriel PM, Partain PT. Parameterization of atmospheric radiative transfer. Part I: vvalidity of simple models. J Atmos Sci 2001;58:3391–409 doi:10.1175/1520-0469(2001)058<3391:POARTP>2.0.CO;2.
[40] Chou M-D, Lee K-T, Tsay S-C, Fu Q. Parameterization for cloud longwave scattering for use in atmospheric models. J Clim 1999;12:159–69. doi:10.1175/1520-0442-12.1.159.
[41] Platnick S, Meyer KG, King MD, Wind G, Amarasinghe N, Marchant B, et al. The MODIS cloud optical and microphysical products: collection 6 updates and examples from terra and Aqua. IEEE Trans Geosci Remote Sens 2017;55:502–25. doi:10.1109/TGRS.2016.2610522.
[42] Platnick S., King M.D., Meyer K.G., Wind G., Amarasinghe N., Marchant B., et al. MODIS cloud optical properties: user guide for the collection 6/6.1 level-2 MOD06/MYD06 product and associated level-3 datasets, Version 1.1, https://modis-atmosphere.gsfc.nasa.gov/sites/default/files/ModAtmo/MODISCloudOpticalPropertyUserGuideFinal_v1.1.pdf; 2018 [accessed 2 August 2019].
[43] Loeb NG, Yang P, Rose FG, Hong G, Sun-Mack S, Minnis P, et al. Impact of ice cloud microphysics on satellite cloud retrievals and broadband flux radiative transfer model calculations. J Clim 2018;31:1851–64. doi:10.1175/JCLI-D-17-0426.1.
[44] Bi L, Yang P. Improved ice particle optical property simulations in the ultraviolet to far-infrared regime. J Quant Spectrosc Radiat Transf 2017;189:228–37. doi:10.1016/j.jqsrt.2016.12.007.
[45] Yang P, Bi L, Baum BA, Liou K-N, Kattawar GW, Mishchenko MI, et al. Spectrally consistent scattering, absorption, and polarization properties of atmospheric ice crystals at wavelengths from 0.2 to 100 μm. J Atmos Sci 2013;70:330–47. doi:10.1175/JAS-D-12-039.1.
[46] Johnson BR. Invariant imbedding T matrix approach to electromagnetic scattering. Appl Opt 1988;27:4861–73. doi:10.1364/AO.27.004861.
[47] Bi L, Yang P. Accurate simulation of the optical properties of atmospheric ice crystals with the invariant imbedding T-matrix method. J Quant Spectrosc Radiat Transf 2014;138:17–35. doi:10.1016/j.jqsrt.2014.01.013.
[48] Yang P, Liou KN. Geometric-optics-integral-equation method for light scattering by nonspherical ice crystals. Appl Opt 1996;35:6568–84. doi:10.1364/AO.35.006568.
[49] Warren SG, Brandt RE. Optical constants of ice from the ultraviolet to the microwave: aa revised compilation. J Geophys Res 2008;113:1–10. doi:10.1029/2007JD009744.
[50] Hong G, Yang P, Baum BA, Heymsfield AJ, Xu K-M. Parameterization of shortwave and longwave radiative properties of ice clouds for use in climate models. J Clim 2009;22:6287–312. doi:10.1175/2009JCLI2844.1.
[51] Yi B, Yang P, Baum BA, L'Ecuyer T, Oreopoulos L, Mlawer EJ, et al. Influence of ice particle surface roughening on the global cloud radiative effect. J Atmos Sci 2013;70:2794–807. doi:10.1175/JAS-D-13-020.1.
[52] Holz RE, Platnick S, Meyer K, Vaughan M, Heidinger A, Yang P, et al. Resolving ice cloud optical thickness biases between CALIOP and MODIS using infrared retrievals. Atmos Chem Phys 2016;16:5075–90. doi:10.5194/acp-16-5075-2016.
[53] Yang P, Hioki S, Saito M, Kuo C-P, Baum B, Liou K-N. A review of ice cloud optical property models for passive satellite remote sensing. Atmosphere (Basel) 2018;9:499. doi:10.3390/atmos9120499.
[54] Downing HD, Williams D. Optical constants of water in the infrared. J Geophys Res 1975;80:1656–61. doi:10.1029/JC080i012p01656.
[55] van de Hulst HC. Light scattering by small particles. New York: Wiley; 1957.
[56] Mitchell DL, Liu Y, Macke A. Modeling cirrus clouds. part II: ttreatment of radiative properties. J Atmos Sci 1996;53:2967–88 doi:10.1175/1520-0469(1996)053<2967:MCCPIT>2.0.CO;2.
[57] He C, Takano Y, Liou K-N, Yang P, Li Q, Chen F. Impact of snow grain shape and black carbon–snow internal mixing on snow optical properties: parameterizations for climate models. J Clim 2017;30:10019–36. doi:10.1175/JCLI-D-17-0300.1.
[58] Chen XH, Huang XL, Flanner MG. Sensitivity of modeled far-IR radiation budgets in polar continents to treatments of snow surface and ice cloud radiative properties. Geophys Res Lett 2014;41:799–804. doi:10.1002/2014GL061216.
[59] Liou K-N. An introduction to atmospheric radiation. 2nd ed. Amsterdam, The Netherlands: Academic Press; 2002.
[60] Wendisch M, Yang P. Theory of atmospheric radiative transfer: a comprehensive introduction. Weinheim: Wiley-VCH; 2012.
[61] Meador WE, Weaver WR. Two-stream approximations to radiative transfer in planetary atmospheres: aa unified description of existing methods and a new improvement. J Atmos Sci 1980;37:630–43 doi:10.1175/1520-0469(1980)037<0630:TSATRT>2.0.CO;2.
[62] Toon OB, McKay CP, Ackerman TP, Santhanam K. Rapid calculation of radiative heating rates and photodissociation rates in inhomogeneous multiple scattering atmospheres. J Geophys Res 1989;94:16287–301. doi:10.1029/JD094iD13p16287.
[63] O'Brien DM, Rikus LJ, Dilley AC, Edwards M. Spectral analysis of infrared heating in clouds computed with two-stream radiation codes. J Quant Spectrosc Radiat Transf 1997;57:725–37. doi:10.1016/S0022-4073(97)00044-7.
[64] Stamnes K, Tsay S-C, Wiscombe W, Jayaweera K. Numerically stable algorithm for discrete-ordinate-method radiative transfer in multiple scattering and emitting layered media. Appl Opt 1988;27:2502–9. doi:10.1364/AO.27.002502.
[65] Henyey LC, Greenstein JL. Diffuse radiation in the galaxy. Astrophys J 1941;93:70–83. doi:10.1086/144246.
[66] Potter JF. The delta function approximation in radiative transfer theory. J Atmos Sci 1970;27:943–9 doi:10.1175/1520-0469(1970)027<0943:TDFAIR>2.0.CO;2.
[67] Joseph JH, Wiscombe WJ, Weinman JA. The delta-Eddington approximation for radiative flux transfer. J Atmos Sci 1976;33:2452–9 doi:10.1175/1520-0469(1976)033<2452:TDEAFR>2.0.CO;2.
[68] Edwards JM. Efficient calculation of infrared fluxes and cooling rates using the two-stream equations. J Atmos Sci 1996;53:1921–32 doi:10.1175/1520-0469(1996)053<1921:ECOIFA>2.0.CO;2.